THESIS FOR THE DEGREE OF DOCTOR OF PHILOSOPHY

Spatiotemporal carrier dynamics in graphene

Roland Jago

CHALMERS

Department of Physics

Chalmers University of Technology

Göteborg, Sweden 2019

Spatiotemporal carrier dynamics in graphene
Roland Jago

ISBN 978-91-7905-100-6

Doktorsavhandlingar vid Chalmers tekniska högskola
Ny serie nr 4567
ISSN 0346-718X

Department of Physics
Chalmers University of Technology
SE-412 96 Göteborg
Sweden
Telephone + 46 (0)31-772 1000

Cover illustration: Spatiotemporal carrier dynamics in graphene

Printed at Chalmers Reproservice
Göteborg, Sweden 2019

Spatiotemporal carrier dynamics in graphene
Roland Jago
Department of Physics
Chalmers University of Technology

Abstract

Graphene as an atomically thin material exhibits remarkable optical and electronic properties that suggest its technological application in novel optoelectronic devices, such as graphene-based photodetectors and lasers. To understand the properties of such devices on a microscopic level, we study the interplay of optical excitation, carrier-carrier, carrier-phonon, and carrier-photon scattering as well as diffusion processes. We apply a microscopic model based on the density matrix formalism with spatiotemporal graphene Bloch equations in its core. This approach provides microscopic access to the temporally, spectrally and spatially resolved carrier dynamics both in the presence and absence of an electric field, allowing the study of many-particle mechanisms behind photodetection and gain in graphene.
The focus of this thesis lies in modelling optics, dynamics and transport phenomena on consistent microscopic footing. We predict the possibility to achieve a stable population inversion in graphene, which is the crucial prerequisite for using graphene as an active material in a nanolaser. Further, we provide microscopic insights into the impact of an electric field on the carrier dynamics revealing the appearance of an efficient dark carrier multiplication that can even enhance the field-induced current. We also provide a microscopic foundation for the photoconduction and the bolometric effect as important mechanisms in a graphene based photodetector. Furthermore, we provide insights into the spatiotemporal dynamics of optically excited carriers, which create density and temperature gradients resulting in a diffusion of carriers. The gained insights can be used to study the thermoelectric effect and dynamics at interfaces of spatial inhomogeneities.

Keywords: graphene, density matrix formalism, Bloch equations, carrier multiplication, relaxation dynamics, photoconduction effect, bolometric effect, spatiotemporal dynamics

List of publications

This thesis consists of an introductory text and the following papers:

First author papers

I. **Spatio-temporal dynamics in graphene**
R. Jago, R. Perea-Causin, S. Brem, and E. Malic
submitted, 2019

II. **Microscopic origin of the bolometric effect in graphene**
R. Jago, E. Malic, and F. Wendler
Phys. Rev. B 99, 035419, 2019

III. **Microscopic understanding of the photoconduction effect in graphene**
R. Jago, F. Wendler and E. Malic
Phys. Rev. B 96, 085431, 2017

IV. **Current enhancement due to field-induced dark carrier multiplication in graphene**
R. Jago, F. Wendler and E. Malic
2D Mater. 4 021031, 2017

V. **Recombination channels in optically excited graphene**
R. Jago, T. Winzer, and E. Malic
Phys. Status Solidi (b), 252:2456-2460, 2015

VI. **Graphene as gain medium for broadband lasers**
R. Jago, T. Winzer, A. Knorr, and E. Malic
Phys. Rev. B, 92:085407, 2015

Co-author papers

VII. **Anomalous optical saturation of low-energy Dirac states in graphene and its implication for nonlinear optics**
B. Semnani, ***R. Jago***, S. Safavi-Naeini. A. H. Majedi, E. Malic, and P. Tassin
arXiv:1806.10123, 2018

VIII. **Unconventional double-bended saturation of carrier occupation in optically excited graphene due to manyparticle interactions**
T. Winzer, M. Mittendorff, S. Winnerl, H. Mittenzwey, ***R. Jago***, M. Helm, E. Malic, and A. Knorr
Nature Commun., 8:15042, 2017

IX. **Carrier Dynamics in Graphene: Ultrafast Many-Particle Phenomena**
E. Malic, T. Winzer, F. Wendler, S. Brem, ***R. Jago***, A. Knorr, M. Mittendorff, J. C. König-Otto, T. Plötzing, D. Neumaier, H. Schneider, M. Helm, S. Winnerl
Annalen der Physik, 1700038, 529, 2017

X. **Ultrafast momentum imaging of pseudospin-flip excitations in graphene**
S. Aeschlimann, R. Krause, M. Chavez-Cervantes, H. Bromberger, ***R. Jago***, E. Malic, A. Al-Temimy, C. Coletti, A. Cavalleri, and I. Gierz
Phys. Rev. B, 96:020301(R), 2017

XI. **Experimentally accessible signatures of Auger scattering in graphene**
T. Winzer, ***R. Jago***, and E. Malic
Phys. Rev. B, 94:235430, 2016

My contributions to the appended papers

I.-VI: As first-author, I developed the theoretical model, performed the numerical evaluation, analyzed the results and wrote the papers with the help of my main supervisor.

VII.-XI.: I contributed by performing specific calculations and helped analyzing the results.

Contents

CHAPTER 1

Methods

1.1 Introduction

Graphene is a two-dimensional material consisting of a monolayer of carbon atoms. For a long time it was assumed that thermodynamic instabilities would prevent the existance of such low-dimensional materials [1]. However, graphene as two-dimensional material was demonstrated first in 2004 by A. Geim and K. S. Novoselov who isolated graphene from graphite within mechanical exfoliation [2]. Only a few years later, in 2010, they received the Nobel prize for their groundbreaking experiments. Graphene exhibits some unique properties among others a vanishing bandgap and a linear band structure in the vicinity of the Dirac point [2, 3], which opens a broad spectrum of new research fields and applications [4].

The linear band structure of graphene enables efficient Auger scattering, which is a two-particle process where one carrier changes the band while the other carrier remains in the band. This results into an increase of carriers, which is quantified by the carrier multiplication (CM). This mechanism has

been theoretically predicted [5–9] and experimentally demonstrated [6, 10–12].

The linear electronic dispersion and the vanishing bandgap provides optically active states in a broad range of frequencies. Together with the high electrical conductivity [3, 13–15], this can be used to build graphene-based photodetectors [16–20] as well as graphene-based saturable absorbers [21–23]. The underlying mechanisms of photodetection can be traced back to the following effects [24, 25]: (i) photoconduction effect which describes the dynamics of optically excited carriers in an external electric field; (ii) the photovoltaic effect which occurs when photo-excited electrons and holes are seperated by an internal electric field, which is generated between differently doped regions; (iii) the bolometric effect which is the change of the conductivity due to the heating of optically excited carriers; (iv) the thermoelectric effect that is important in the presence of a temperature gradient, which is transformed by the Seebeck effect into a photocurrent. Under certain conditions different mechanisms dominate the dynamics of the photocurrent. In graphene-metal and metal-graphene-metal junctions [17, 26–28] the photovoltaic effect is the driving mechanism, in the case without external bias [29–32] the thermoelectric effect dominates and under bias the photoconduction and the photobolometric effect determine the behaviour of the photocurrent [33–36]. In this thesis the focus lies on the explanation of the photoconduction and the bolometric effect. Furthermore, we study spatio-temporal carrier dynamics which are prerequisites for the photovoltaic and thermoelectric effect, since these effect does not occur in a spatial homomgeneous system.

The aim of the thesis is to describe and understand the spatio-temporal carrier dynamics and transport phenomena in graphene. The transport phenomena studied in this thesis appear either due to an external electric field or are diffusion induced. To get insight into the complex mechanisms, the general non-equilibrium carrier dynamics in a spatial homogeneous system without transport is investigated in chapter 2. A non-equilibrium situation can be achieved by optical excitation of carriers. Due to many-particle scattering the carriers thermalize and relax back into the initial carrier distribution, cf. Fig. 1.1(a). Since graphene exhibits excellent conditions for Auger processes, carrier multiplication (CM) occurs, which means that optically excited carriers generate additional carriers. In chapter 3 the case with no optical excitation is considered and the impact of an external electric field on

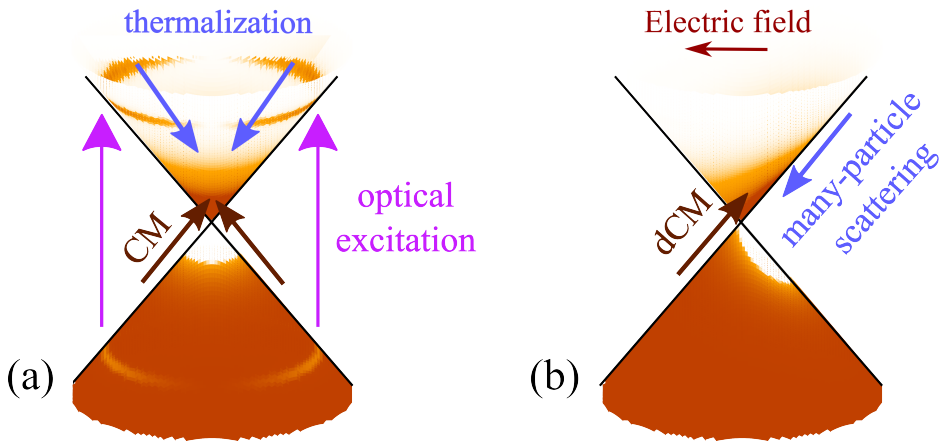

Figure 1.1: *(a) Optically excited carriers thermalize. During the thermalization they create additional carriers due to carrier multiplication (CM). (b) An electric field shifts carriers which scatter back via many-particle processes and similar to (a) they induce dark carrier multiplication (dCM).*

the carrier dynamics is determined, cf. Fig. 1.1 (b). The field induced shift of carriers leads to an asymmetric carrier distribution. Note that the carriers are shifted in the opposite direction compared to the field since the electron charge is negative. The many-particle scattering acts against the field such that a quasi-equilibrium can be achieved and a dark current is formed. Again, Auger scattering increases the number of carriers (this time in the absence of optical light), which is denoted by dark carrier multiplication (dCM). In chapter 4 the influence of both effects, optical excitation and applied electric field, to the carrier dynamics, which means the photoconduction effect, is discussed. Later on the investigations are extended to determine the bolometric effect in chapter 5. The properties of the obtained photocurrents give insights into the modelling of graphene-based photodetectors. Finally, the dynamics of optical excited carriers for spatial inhomogeneous systems and the impact of diffusion processes are discussed in chapter 6.

1.2 Hamilton operator

The microscopic properties of optically excited graphene in the presence of an electric field by including carrier-carrier and carrier-phonon scattering are described by the many-particle Hamilton operator [37, 38]

$$H = H_0 + H_{c,c} + H_{c,ph} + H_{c,l} + H_{c,f}. \tag{1.1}$$

Here, H_0 is the free Hamilton operator of carriers and phonons, $H_{c,c}$ and $H_{c,ph}$ describe the carrier-carrier and carrier-phonon interactions, $H_{c,l}$ is the carrier-light coupling which is treated on a semi-classical level and $H_{c,f}$ describes the influence of an external electric field on the carriers. In second quantization the carriers can be expressed with creation and annihilation operators $a^\dagger_{\mathbf{k}\lambda}$ and $a_{\mathbf{k}\lambda}$, with the wave vector $\mathbf{k}$ and the bandindex $\lambda \in \{v,c\}$ (valence and conduction band). The phonon operators are $b^\dagger_{\mathbf{q}j}$ and $b_{\mathbf{q}j}$ with the momentum $\mathbf{q}$ and the phonon mode j including optical and acoustic modes.
The free Hamilton operator reads

$$H_0 = \sum_{\mathbf{k}\lambda} \varepsilon^\lambda_{\mathbf{k}} a^\dagger_{\mathbf{k}\lambda} a_{\mathbf{k}\lambda} + \sum_{\mathbf{q}j} \hbar\omega_{\mathbf{q}j} b^\dagger_{\mathbf{q}j} b_{\mathbf{q}j}, \tag{1.2}$$

where $\varepsilon^\lambda_{\mathbf{k}}$ denotes the electronic band structure of graphene and $\omega_{\mathbf{q}j}$ is the phonon frequency. The Hamilton operators for the carrier-phonon and carrier-carrier interactions accounting for phonon- and Coulomb-induced intraband scattering and non-radiative recombination processes are given by

$$H_{c,ph} = \sum_{\lambda\lambda'\mathbf{k}} \sum_{\mathbf{q}j} \left(g^{\lambda\lambda'}_{\mathbf{kq}j}\, a^\dagger_{\mathbf{k}\lambda} a_{\mathbf{k}-\mathbf{q},\lambda'} b_{\mathbf{q}j} + \text{h.c.} \right) \tag{1.3}$$

$$H_{c,c} = \frac{1}{2} \sum_{\mathbf{1234}} V^{\mathbf{12}}_{\mathbf{34}} a^\dagger_{\mathbf{1}} a^\dagger_{\mathbf{2}} a_{\mathbf{4}} a_{\mathbf{3}}, \tag{1.4}$$

with the carrier-phonon matrix element $g^{\lambda\lambda'}_{\mathbf{kq}j}$ and the Coulomb matrix element $V^{\mathbf{12}}_{\mathbf{34}}$, h.c. stands for Hermitian conjugate. The multi-indices **1**,**2**,**3**,**4** include carrier momenta and band index. The Hamilton operator for the carrier-light interaction is:

$$H_{c,l} = i\frac{e_0\hbar}{m_0} \sum_{\lambda\lambda'\mathbf{k}} \mathbf{A}(t) \cdot \mathbf{M}^{\lambda\lambda'}_{\mathbf{k}}\, a^\dagger_{\mathbf{k}\lambda} a_{\mathbf{k}\lambda'}, \tag{1.5}$$

with the free electron mass m_0 and the free electron charge e_0. The carrier-light coupling matrix element $\mathbf{M}_{\mathbf{k}}^{vc} = \langle \mathbf{k}\lambda | \nabla | \mathbf{k}\lambda' \rangle$[39, 40] describes the interaction between electrons and an external optical field, which is characterized by the vector potential $\mathbf{A}(t)$.

The interaction of an external electric field (which is in the plane of the graphene sheet) with the carriers can be derived by starting from the Hamilton operator for the external electrostatic potential Φ,

$$H_{c,f} = -e_0 \sum_{\mathbf{12}} \langle \mathbf{1} | \Phi | \mathbf{2} \rangle a_{\mathbf{1}}^{\dagger} a_{\mathbf{2}}, \tag{1.6}$$

with Bloch states $\langle \mathbf{1}|$ and $|\mathbf{2}\rangle$. A possible representation of the electrostatic potential is given by $\Phi = -\mathbf{r} \cdot \mathbf{E}$ with the electric field $\mathbf{E}$. The product of the position operator $\mathbf{r}$ with the exponential factor of the Bloch state $e^{i\mathbf{r}\cdot\mathbf{k}_2}$ can be rewritten into $\mathbf{r}e^{i\mathbf{r}\cdot\mathbf{k}_2} = -i\nabla_{\mathbf{k}_2} e^{i\mathbf{r}\cdot\mathbf{k}_2}$ and after a partial integration in $\mathbf{k}_2$ the carrier-field Hamilton operator finally reads

$$H_{c,f} = -ie_0 \mathbf{E} \sum_{\mathbf{k}\lambda} a_{\mathbf{k}\lambda}^{\dagger} \nabla_{\mathbf{k}} a_{\mathbf{k}\lambda}. \tag{1.7}$$

1.3 Band structure and matrix elements

In this section the band structure of graphene as well as all coupling matrix elements (for the carrier-phonon, Coulomb and carrier-light interactions) will be derived.

Band structure of graphene

Lattice structure

Graphene is a two-dimensional honeycomb structure consisting of carbon atoms. The unit cell is build-up with two equivalent sub-lattices A and B, which are rotated to each other by an angle of $\pi/3$, cf. Fig. 1.2a). The unit cell is defined by the vectors $\mathbf{a}_1 = \frac{a_0}{2}(\sqrt{3},1)$ and $\mathbf{a}_2 = \frac{a_0}{2}(\sqrt{3},-1)$ with the lattice constant $a_0 = 0.246\,\mathrm{nm}$, the area of the unit cell is given by

$A_{uc} = \sqrt{3}a_0^2/2$. The corresponding reciprocal lattice is shown in Fig. 1.2b) and is defined by the vectors $\mathbf{k}_1 = \frac{2\pi}{a_0\sqrt{3}}(1,\sqrt{3})$ and $\mathbf{k}_2 = \frac{2\pi}{a_0\sqrt{3}}(1,-\sqrt{3})$. The high symmetry points are Γ, M, K and K'. The vectors $\mathbf{b}_1 = \frac{a_0}{2\sqrt{3}}\big(-1,\sqrt{3}\big)$, $\mathbf{b}_2 = \frac{a_0}{\sqrt{3}}\big(1,0\big)$ and $\mathbf{b}_3 = \frac{a_0}{2\sqrt{3}}\big(-1,-\sqrt{3}\big)$ connect one atom from the A-lattice with the three nearest neighbour atoms in the B-lattice, cf. Fig. 1.2 (a).

Band structure

The starting point to compute the electronic band structure of graphene is the stationary Schrödinger equation

$$H_{0,c}|\psi_{\mathbf{k}}(\mathbf{r})\rangle = \varepsilon_{\mathbf{k}}|\psi_{\mathbf{k}}(\mathbf{r})\rangle, \tag{1.8}$$

with the free electronic Hamilton operator $H_{0,c}$. The electronic properties of graphene are mainly determined by the p_z orbitals. Due to the localization of these atomic orbitals, the electronic wave function $|\psi_{\mathbf{k}}(\mathbf{r})\rangle$ can be written with a tight-binding Ansatz [41, 42] as a linear combination of the two wave functions of the sub-lattices A and B

$$|\psi_{\mathbf{k}}(\mathbf{r})\rangle = c_A(\mathbf{k})|\Phi_{A,\mathbf{k}}(\mathbf{r})\rangle + c_B(\mathbf{k})|\Phi_{B,\mathbf{k}}(\mathbf{r})\rangle, \tag{1.9}$$

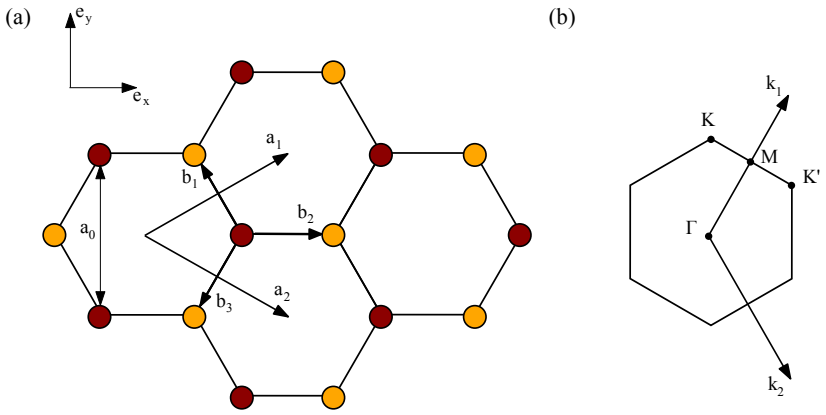

Figure 1.2: *(a) The unit cell of graphene with the sub-lattices A (orange dots) and B (red dots) is defined by the vectors $\mathbf{a}_1$ and $\mathbf{a}_2$. The $\mathbf{b}_i$ are vectors from one atom A to the three nearest neighbours in the B-lattice. (b) The first Brillouin zone of graphene is defined by $\mathbf{k}_1$ and $\mathbf{k}_2$, with the high symmetry points Γ, M, K and K'.*

where $|\Phi_{j,\mathbf{k}}(\mathbf{r})\rangle$ is the wave function of the sub-lattice $j \in \{A,B\}$ and $c_i(\mathbf{k})$ are the corresponding tight-binding coefficients. The eigenstates $|\phi(\mathbf{r}-\mathbf{R}_j)\rangle$ and eigenenergies of the isolated atomic orbitals are known, and by linear combination a Bloch state for the sublattices $i = A,B$ can be constructed,

$$|\Phi_{j,\mathbf{k}}(\mathbf{r})\rangle = \frac{1}{\sqrt{N}} \sum_{\mathbf{R}_j} e^{i\mathbf{k}\mathbf{R}_j} |\phi(\mathbf{r}-\mathbf{R}_j)\rangle, \tag{1.10}$$

where N is the number of unit cells in the system. To solve the Schrödinger equation (1.8) analytically, this equation is separately multiplied with $\langle\Phi_{A,\mathbf{k}}(\mathbf{r})|$ and $\langle\Phi_{B,\mathbf{k}}(\mathbf{r})|$, which leads to the system of equations

$$\begin{pmatrix} H_{AA}-\varepsilon_{\mathbf{k}}S_{AA} & H_{AB}-\varepsilon_{\mathbf{k}}S_{AB} \\ H_{BA}-\varepsilon_{\mathbf{k}}S_{BA} & H_{BB}-\varepsilon_{\mathbf{k}}S_{BB} \end{pmatrix} \begin{pmatrix} c_A \\ c_B \end{pmatrix} = 0, \tag{1.11}$$

with the defintions $H_{ij} = \langle\Phi_{i,\mathbf{k}}(\mathbf{r})|H_{0,c}|\Phi_{j,\mathbf{k}}(\mathbf{r})\rangle$ and $S_{ij} = \langle\Phi_{i,\mathbf{k}}(\mathbf{r})|\Phi_{j,\mathbf{k}}(\mathbf{r})\rangle$. Because of the equivalence of the sub-lattices and the symmetry properties of the scalar product, it holds $(H/S)_{AA} = (H/S)_{BB}$ and $(H/S)_{AB} = (H/S)^*_{BA}$. To get non-trivial solutions, the secular determinante has to vanish and the eigenvalues reads

$$\varepsilon_{\mathbf{k}\lambda} = E_{\mathbf{k}} \pm \sqrt{E_{\mathbf{k}} - H_{AA}^2 + |H_{AB}|^2} \tag{1.12}$$

with

$$E_{\mathbf{k}} = \frac{H_{AA}S_{AA} - \mathrm{Re}\big[H_{AB}S^*_{AB}\big]}{S_{AA}^2 - |S_{AB}|^2}. \tag{1.13}$$

The positive sign stands for $\lambda = v$ (valence band) and the negative sign stands for $\lambda = c$ (conduction band). In the next step the matrix elements will be determined within the tight-binding approximation. From (1.10) we have

$$H_{AB} = \frac{1}{N} \sum_{\mathbf{R}_A\mathbf{R}_B} e^{i\mathbf{k}\left(\mathbf{R}_B-\mathbf{R}_A\right)} \langle\phi(\mathbf{r}-\mathbf{R}_A)|H|\phi(\mathbf{r}-\mathbf{R}_B)\rangle. \tag{1.14}$$

Due to the strong localization of the atomic wave functions, the sum can be computed with the nearest neighbour approximation. That means that the sum contains for each atom from the A sub-lattice only the three nearest neighbours from the B sub-lattice with $\mathbf{R}_B = \mathbf{R}_A + \mathbf{b}_i$, where $\mathbf{b}_i$, $i = 1,2,3$

are the vectors between nearest neighbours, depicted in Fig. 1.2 (a). It follows

$$H_{AB} = \frac{1}{N}\sum_{\mathbf{R}_A}\sum_{i=1}^{3} e^{i\mathbf{k}\mathbf{b}_i}\langle\phi(\mathbf{r}-\mathbf{R}_A)|H|\phi(\mathbf{r}-\mathbf{R}_A-\mathbf{b}_i)\rangle$$

$$= \gamma_0 e(\mathbf{k}), \tag{1.15}$$

with the constant integral $\gamma_0 = \langle\phi(\mathbf{r}-\mathbf{R}_A)|H|\phi(\mathbf{r}-\mathbf{R}_A-\mathbf{b}_i)\rangle$ and the function $e(\mathbf{k})$ defined by

$$e(\mathbf{k}) = \sum_{i=1}^{3} e^{i\mathbf{k}\mathbf{b}_i}, \tag{1.16}$$

which contains the symmetries of the lattice structure. The values for γ_0 are in the range from $-2.7\,\mathrm{eV}$ to $-3.3\,\mathrm{eV}$ [43–45], in this work a value of $\gamma_0 = -2.84\,\mathrm{eV}$ is assumed. All other matrix elements can be determined analogous, such as $H_{AA} = \varepsilon_0 = const.$, which is chosen to be $\varepsilon_0 = 0\,\mathrm{eV}$, taking into account that only relative energy values to the fermi level can be measured. With normalized eigenfunctions $|\Phi_{j,\mathbf{k}}(\mathbf{r})\rangle$, $S_{AA} = 1$ follows directly. S_{AB}, which describes the overlap between neighboring atomic orbitals, is given by

$$S_{AB} = s_0 e(\mathbf{k}), \tag{1.17}$$

with the overlap integral $s_0 = \langle\phi(\mathbf{r}-\mathbf{R}_A)|\phi(\mathbf{r}-\mathbf{R}_A-\mathbf{b}_i)\rangle$. Finally, the band structure reads

$$\varepsilon_{\mathbf{k},v/c} = \frac{\pm\gamma_0|e(\mathbf{k})|}{1 \pm s_0|e(\mathbf{k})|}, \tag{1.18}$$

and is shown in Fig. 1.3. The value of s_0 can be computed numerically within the p_z-orbitals and an effective atomic charge number, which gives $s_0 = 0.07$. This overlap integral will be neglected in the following sections, which provides a good description in the linear energy regime. The evaluation of the function $|e(\mathbf{k})|$ yields

$$|e(\mathbf{k})| = \sqrt{3 + 4\cos\left(\frac{a_0}{2}k_y\right)\cos\left(\frac{a_0\sqrt{3}}{2}k_x\right) + 2\cos\left(a_0 k_y\right)}. \tag{1.19}$$

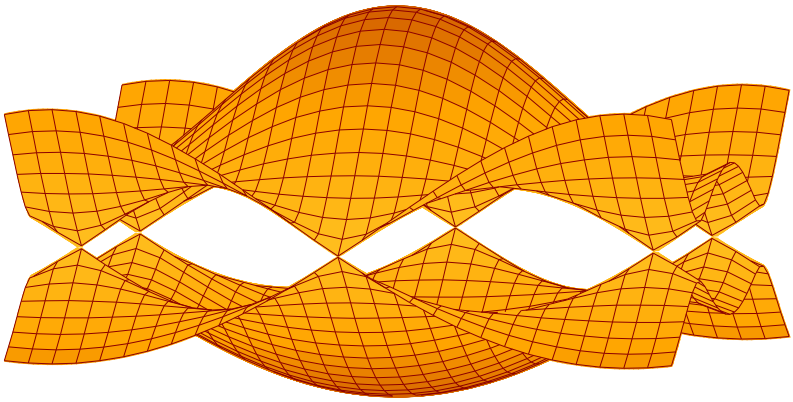

Figure 1.3: *Band structure of graphene containing the conduction and the valence band of the first Brillouin zone. Around the K-point is the band structure linear and gapless. The energy is maximal at the Γ-point and has at the M-point a saddle.*

Linearized band structure

At the Dirac point the valence band touches the conduction band and the band structure can be linearly approximated. Using a Taylor expansion around the K-point with $\mathbf{K} = (0, \frac{4\pi}{3a_0})$ yields

$$e(\mathbf{k}) \approx e(\mathbf{K}) + \nabla e(\mathbf{k}+\mathbf{K})|_{\mathbf{k}=0} \cdot \mathbf{k} = \nabla e(\mathbf{k}+\mathbf{K})|_{\mathbf{k}=0} \cdot \mathbf{k} \tag{1.20}$$

$$\nabla e(\mathbf{k}+\mathbf{K})|_{\mathbf{k}=0} = i \sum_{i=1}^{3} \mathbf{b}_i \, e^{i\mathbf{b}_i \mathbf{K}}. \tag{1.21}$$

Evaluation of the sum leads to $|e(\mathbf{k})| = \frac{\sqrt{3}a_0}{2}|\mathbf{k}|$ and the linear band structure reads

$$\varepsilon_{\mathbf{k}}^{\lambda} = \mp \hbar v_F |\mathbf{k}|, \tag{1.22}$$

with the Fermi velocity $v_F = -\gamma_0 \frac{\sqrt{3}a_0}{2\hbar} \approx 0.92 \, \frac{\text{nm}}{\text{fs}}$.

Carrier-phonon matrix element

In this work optical and acoustic phonon modes are considered, explicitly the ΓLO, ΓTO, KTO and ΓLA phonon modes. The dispersion of the optical modes can be approximated by constants [46], $\hbar\omega_{\Gamma LO} = 198\,\mathrm{meV}$, $\hbar\omega_{\Gamma TO} = 192\,\mathrm{meV}$ and $\hbar\omega_{KTO} = 162\,\mathrm{meV}$. The optical phonons induce inter- and intraband scattering of electrons. The Γ-modes account for intravalley scattering and the K-phonons induce intervalley scattering. The acoustic phonon mode dispersion is approximately linear and is given by $\hbar\omega_{\Gamma LA} = v_{\Gamma LA}\,|\mathbf{q}|$ with the phonon momentum $\mathbf{q}$. Since $v_{\Gamma LA} < v_F$, only intraband scattering of electrons is possible. The electron-phonon matrix elements have the explicit forms[47–49]

$$|g^{\lambda\lambda'}_{\mathbf{kq},\Gamma LO}|^2 = |g^{\lambda\lambda}_{\mathbf{kq},\Gamma TO}|^2 = \frac{1}{N}\langle g^2_{\Gamma O}\rangle\big[1+\cos\big(\theta+\theta'\big)\big], \tag{1.23}$$

$$|g^{\lambda\lambda'}_{\mathbf{kq},\Gamma TO}|^2 = |g^{\lambda\lambda}_{\mathbf{kq},\Gamma LO}|^2 = \frac{1}{N}\langle g^2_{\Gamma O}\rangle\big[1-\cos\big(\theta+\theta'\big)\big], \tag{1.24}$$

$$|g^{\lambda\lambda'}_{\mathbf{kq},K-TO}|^2 = \frac{1}{N}\langle g^2_{KO}\rangle\big[1-\sigma_{\lambda\lambda'}\cos\big(\theta''\big)\big], \tag{1.25}$$

$$|g^{\lambda\lambda}_{\mathbf{kq},\Gamma LA}|^2 = \frac{1}{L^2}\langle g^2_{\Gamma A,\mathbf{q}}\rangle\big[1+\cos\big(\theta''\big)\big], \tag{1.26}$$

with the constants $\langle g^2_{\Gamma O}\rangle = 0.0994\,\mathrm{eV}^2$, $\langle g^2_{KO}\rangle = 0.0405\,\mathrm{eV}^2$ and $\langle g^2_{\Gamma A,\mathbf{q}}\rangle = q^2D^2\omega_{\mathbf{q},\Gamma LA}/\rho_m$, where $D = 16\,\mathrm{eV}$ is the deformation potential and $\rho_m = 7.6\cdot10^{-8}\,\mathrm{gcm}^{-2}$ describes the mass density of graphene. N is the number of unit cells, L^2 is the area of the graphene sheet, θ is the scattering angle between $\mathbf{k}$ and $\mathbf{q}$, θ' is the angle between $\mathbf{k}+\mathbf{q}$ and $\mathbf{q}$, and θ'' is the angle between $\mathbf{k}$ and $\mathbf{k}+\mathbf{q}$.

Coulomb matrix element

The Coulomb matrix element determines the strength of carrier-carrier scattering and reads [38]

$$V_{\mathbf{34}}^{\mathbf{12}} = \int\int d\mathbf{r}d\mathbf{r}'\, \psi_{\mathbf{1}}^*(\mathbf{r})\psi_{\mathbf{2}}^*(\mathbf{r}')V(\mathbf{r}-\mathbf{r}')\psi_{\mathbf{4}}(\mathbf{r}')\psi_{\mathbf{3}}(\mathbf{r}), \tag{1.27}$$

with the multi indices $\mathbf{i} = \left(\mathbf{k}_i, \lambda_{\mathbf{i}}\right)$, the Coulomb potential $V(\mathbf{r}-\mathbf{r}') = \frac{e^2}{4\pi\epsilon_0}\frac{1}{|\mathbf{r}-\mathbf{r}'|}$ and the graphene tight-binding wave functions $\psi_{\mathbf{i}}$. To determine the Coulomb matrix element, effective $2\,p_z$ hydrogen orbital functions corresponding to an effective charge number Z_{eff} are applied. In the nearest neighbour approximation the Coulomb matrix element can be expressed as [37, 39]

$$V_{\mathbf{34}}^{\mathbf{12}} = V_{\mathbf{q}}\left[\left(\frac{qa_B}{Z_{eff}}\right)^2 + 1\right]^{-6} \alpha_{\mathbf{34}}^{\mathbf{12}}\,\delta_{\mathbf{k}_1+\mathbf{k}_2,\mathbf{k}_3+\mathbf{k}_4}, \tag{1.28}$$

with the Bohr radius a_B, the Fourier transform $V_{\mathbf{q}} = \frac{e^2}{2\,\epsilon_0 L^2}\frac{1}{q}$ of the two-dimensional Coulomb potential and the transfer momentum $q = |\mathbf{k}_3 - \mathbf{k}_1|$ of the interacting carriers. The energy and momentum conservation is described by the Kronecker delta, which means that the sum of momenta of the initial states **3**,**4** has to equal the sum for the final states **1**,**2**. The form factor $\alpha_{\mathbf{34}}^{\mathbf{12}}$ is given by

$$\alpha_{\mathbf{34}}^{\mathbf{12}} = \frac{1}{4}\left(1 + \sigma_{\lambda_1\lambda_3}\frac{e^*(\mathbf{k}_1)e(\mathbf{k}_3)}{|e(\mathbf{k}_1)||e(\mathbf{k}_3)|}\right)\cdot\left(1 + \sigma_{\lambda_2\lambda_4}\frac{e^*(\mathbf{k}_2)e(\mathbf{k}_4)}{|e(\mathbf{k}_2)||e(\mathbf{k}_4)|}\right), \tag{1.29}$$

where $\sigma_{\lambda\lambda'}$ is equal to $+1$ for intraband processes ($\lambda = \lambda'$) and -1 for interband processes ($\lambda \neq \lambda'$).

Screening

The Coulomb potential is screened by the substrate as well as by the carriers in graphene. It is assumed that the substrate with the dielectric constant ε_{sub} is only on one side of graphene and on the other side is vacuum, resulting into

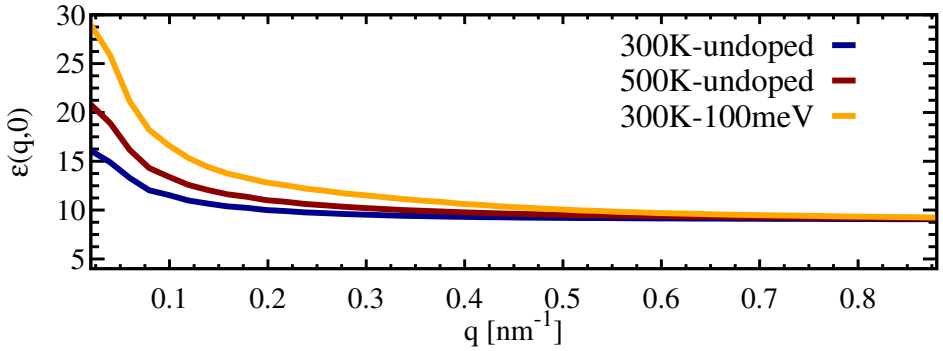

Figure 1.4: *Lindhard screening for initial carrier distributions with different temperatures and doping. The increase of carriers, either with higher temperatures or with doping, results into a larger screening for small momentum transfers.*

the averaged background dielectric constant $\varepsilon_{bg} = (\varepsilon_{sub} + \varepsilon_{vac})/2$. The carrier induced screening $\varepsilon(\mathbf{q},t)$ is determined by the static Lindhard formula [38]

$$\varepsilon(\mathbf{q},t) = 1 - 2\,\frac{V_\mathbf{q}}{\varepsilon_{bg}} \sum_{\mathbf{k},\lambda\lambda'} \frac{\rho^\lambda_\mathbf{k}(t) - \rho^{\lambda'}_{\mathbf{k-q}}(t)}{\varepsilon^\lambda_\mathbf{k} - \varepsilon^{\lambda'}_{\mathbf{k-q}}} \left|C^{\lambda\lambda'}_\mathbf{q}(\mathbf{k})\right|^2, \tag{1.30}$$

with the form factor $C^{\lambda\lambda'}_\mathbf{q}(\mathbf{k}) = \int d\mathbf{r} \psi^*_\lambda(\mathbf{k}) e^{-i\mathbf{qr}} \psi_{\lambda'}(\mathbf{k})$. The time dependence of the carrier distribution $\rho^\lambda_\mathbf{k}(t)$ is explicitly taken into account by solving the graphene Bloch equations. The screened Coulomb potential reads $\tilde{V}_q = V_q/\varepsilon_{bg}\varepsilon(\mathbf{q},t)$.

Optical matrix element

The optical matrix element $\mathbf{M}^{\lambda\lambda'}_{\mathbf{kk'}}$ for the electronic momenta $\mathbf{k}$, $\mathbf{k}'$ and the band index λ, λ' within the minimal coupling gauge is given by [37, 50]

$$\mathbf{M}^{\lambda\lambda'}_{\mathbf{kk'}} = \langle \mathbf{k}\,\lambda | \nabla | \mathbf{k}'\,\lambda' \rangle. \tag{1.31}$$

Using the tight-binding wave functions of graphene in nearest neighbour approximation (cf. section 1.3) and exploiting the symmetries of the $2\,p_z$-

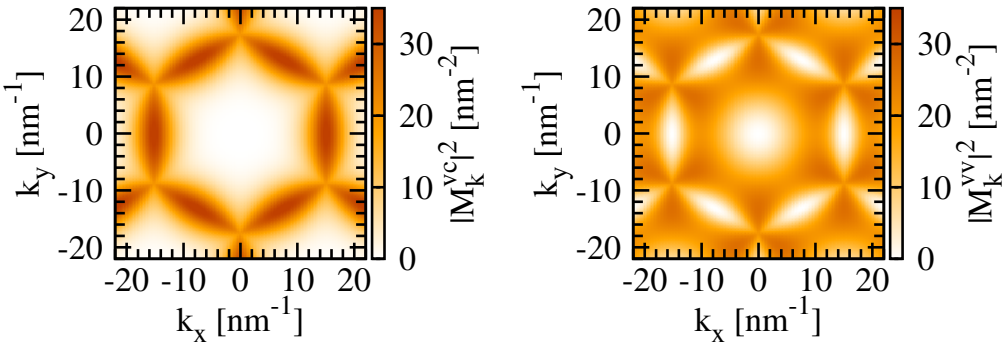

Figure 1.5: *Square of the absolute value of the interband matrix element* $|\mathbf{M}_{\mathbf{k}}^{vc}|^2$ *with a maximum at the* M *point it vanishes at the* Γ *point. At the* K *point the interband matrix element has the same strength as the intraband matrix element* $|\mathbf{M}_{\mathbf{k}}^{vv}|^2$.

orbitals, the following form of the optical matrix element can be obtained

$$\mathbf{M}_{\mathbf{k}\mathbf{k}'}^{vv} = \frac{iM\delta_{\mathbf{k}\mathbf{k}'}}{|\mathbf{b}_1||e(\mathbf{k})|}\,\mathrm{Im}\left(e^*(\mathbf{k})\sum_{i=1}^{3}e^{i\mathbf{k}\mathbf{b}_i}\mathbf{b}_i\right) = -\mathbf{M}_{\mathbf{k}\mathbf{k}'}^{cc} \tag{1.32}$$

$$\mathbf{M}_{\mathbf{k}\mathbf{k}'}^{vc} = \frac{M\delta_{\mathbf{k}\mathbf{k}'}}{|\mathbf{b}_1||e(\mathbf{k})|}\,\mathrm{Re}\left(e^*(\mathbf{k})\sum_{i=1}^{3}e^{i\mathbf{k}\mathbf{b}_i}\mathbf{b}_i\right) = -\mathbf{M}_{\mathbf{k}\mathbf{k}'}^{cv}, \tag{1.33}$$

with the constant $M \approx 3\,\mathrm{nm}^{-1}$. The Kronecker delta $\delta_{\mathbf{k}\mathbf{k}'}$ results from the dipol approximation and reflects the neglection of the photon momentum, i.e. only direct optical transitions are allowed. In the following $\mathbf{M}_{\mathbf{k}\mathbf{k}'}^{\lambda\lambda'} = \mathbf{M}_{\mathbf{k}}^{\lambda\lambda'}\,\delta_{\mathbf{k}\mathbf{k}'}$ is used.

Linear approximation

The band structure of graphene around the Dirac point is linear. Using this, the optical matrix element can be expanded to give

$$\mathbf{M}_{\mathbf{k}}^{vc} \approx \frac{3}{2}\,M\,\hat{\mathbf{e}}_{\phi} \qquad \text{and} \qquad \mathbf{M}_{\mathbf{k}}^{vv} \approx -\frac{3}{2}i\,M\,\hat{\mathbf{e}}_{k}, \tag{1.34}$$

with the unit vectors $\hat{\mathbf{e}}_k$ and $\hat{\mathbf{e}}_{\phi}$.

1.4 Spatio-temporal Bloch equations

The dynamics of carriers in graphene are described by the following microscopic quantities: (i) the carrier occupation $\rho_{\mathbf{k}}^{\lambda} = \langle a_{\mathbf{k}\lambda}^{\dagger} a_{\mathbf{k}\lambda} \rangle$ in valence and conduction band, (ii) the microscopic polarisation $p_{\mathbf{k}} = \langle a_{\mathbf{k}v}^{\dagger} a_{\mathbf{k}c} \rangle$ which measures the probability of an electronic transition, and (iii) the phonon number $n_{\mathbf{q}}^{j} = \langle b_{\mathbf{q}j}^{\dagger} b_{\mathbf{q}j} \rangle$. The carrier occupation of holes in the valence band is defined as $\rho_{\mathbf{k}}^{h} = 1 - \rho_{\mathbf{k}}^{v}$. The time evolution is derived with the Heisenberg equations of motions [38], for example $\dot{\rho}_{\mathbf{k}}^{\lambda} = \frac{i}{\hbar} \langle [H, a_{\mathbf{k}\lambda}^{\dagger} a_{\mathbf{k}\lambda}] \rangle$. To get a closed set of equations it is necessary to apply some approximations.

Approximations

Correlation expansion

Equations which are derived within the density matrix formalism have a hierarchy problem. This means that n-particle expectation values couple to n+1-particle expectation values, i.e. solving a dynamical system needs to consider an infinitly hierarchy of equations. The essential idea of the correlation expansion [51, 52] is to factorize a n-particle expectation value in all possible ways into correlations, which are denoted with $\langle ... \rangle^{c}$. To get a finite system of equations for n particles, all correlations including n or more particles will be neglected. The correlation expansion up to the second-order (also known as second-order Born approximation) is given by

$$\langle 1 \rangle = \langle 1 \rangle^{c} \tag{1.35}$$

$$\langle 2 \rangle = \sum_{\sigma \in \Pi} (-1)^{\sigma_f} \langle 1 \rangle \langle 1' \rangle + \langle 2 \rangle^{c}, \tag{1.36}$$

where the occuring sum includes all possible permutations σ of one particle expectation values. Every fermionic permutation changes the sign, which is taking into account by the pre-factor $(-1)^{\sigma_f}$ with the number of fermionic permutations σ_f. For example, the correlation expansion in second-order for electrons (by neglecting the two-particle correlation) is called Hartree-Fock approximation and reads $\langle a_i^{\dagger} a_j^{\dagger} a_k a_l \rangle \approx \langle a_i^{\dagger} a_l \rangle \langle a_j^{\dagger} a_k \rangle - \langle a_i^{\dagger} a_k \rangle \langle a_j^{\dagger} a_k \rangle$.

Markov approximation

Within the Markov approximation it is possible to simplify the system of equations by solving the equation for a n+1-particle. The obtained analytical solution is then inserted into the equation of motion for a n-particles. In this approximation memory effects are neglected. A differential equation of the following form can be solved with the Markov approximation

$$\frac{d}{dt}f(t) = -\big(i\omega + \Gamma\big)f(t) + i\,Q(t), \tag{1.37}$$

with a free oscillating part $i\omega$, a damping $-\Gamma$ and an inhomogeneity $Q(t)$. A formal integration of this equation with $f(t \to -\infty) = 0$ yields

$$f(t) = i\int_{-\infty}^{t} dt'\,Q(t')\,e^{-\big(i\omega+\Gamma\big)\big(t-t'\big)} = i\int_{0}^{\infty} ds\,Q(t-s)\,e^{-\big(i\omega+\Gamma\big)s}. \tag{1.38}$$

In the last step the substitution $s = t - t'$ was used. In the Markov approximation, the inhomogeneity is split up into a fast oscillating term $e^{i\omega' s}$ and a slow oscillating term $\tilde{Q}(t)$. The slow part is now independent of s, therefore it be taken out of the integral and the integral results into

$$f(t) = \tilde{Q}(t)\left(i\frac{\Gamma}{\Delta\omega^2+\Gamma^2} - \frac{\Delta\omega}{\Delta\omega^2+\Gamma^2}\right), \tag{1.39}$$

with the abbreviation $\Delta\omega = \omega' - \omega$. The second term is the principal value and will be neglected in the following. The first term describes a Lorentz profile with width Γ. For vanishing damping, i.e. $\Gamma \to 0$, energy preservation holds and is described by a delta function [53]

$$f(t) = i\pi\,\tilde{Q}(t)\,\delta\big(\Delta\omega\big). \tag{1.40}$$

Many-particle scattering

The relaxation of non-equilibrium carriers is driven by carrier-phonon and Coulomb induced relaxation processes, which can influence non-radiative recombination of carriers.

Carrier-phonon scattering

The impact of phonons to the carrier occupation leads to scattering equations for the carriers and the phonons. Starting from the Heisenberg equation of motion, the dynamical equations for the carrier occupation (the equation for the polarisation can be derived in an analogous way) and the phonon number are given by

$$\dot{\rho}^{\lambda}_{\mathbf{k}}\big|_{H_{c,ph}} = -\frac{i}{\hbar}\sum_{\mathbf{q}j}\sum_{\lambda'}\Big[g^{\lambda\lambda'}_{\mathbf{kq}j}\,\langle a^{\dagger}_{\mathbf{k}\lambda}a_{\mathbf{k}-\mathbf{q},\lambda'}b_{\mathbf{q}j}\rangle - g^{\lambda'\lambda}_{\mathbf{k}+\mathbf{q},\mathbf{q}j}\,\langle a^{\dagger}_{\mathbf{k}+\mathbf{q},\lambda'}a_{\mathbf{k}\lambda}b_{\mathbf{q}j}\rangle + g^{\lambda'\lambda *}_{\mathbf{k}+\mathbf{q},\mathbf{q}j}\,\langle a^{\dagger}_{\mathbf{k}\lambda}a_{\mathbf{k}+\mathbf{q},\lambda'}b^{\dagger}_{\mathbf{q}j}\rangle - g^{\lambda\lambda' *}_{\mathbf{kq}j}\,\langle a^{\dagger}_{\mathbf{k}-\mathbf{q},\lambda'}a_{\mathbf{k}\lambda}b^{\dagger}_{\mathbf{q}j}\rangle\Big], \tag{1.41}$$

$$\dot{n}^{j}_{\mathbf{q}}\big|_{H_{c,ph}} = -\frac{i}{\hbar}\sum_{\mathbf{k}}\sum_{\lambda\lambda'}\Big[g^{\lambda\lambda'}_{\mathbf{kq}j}\,\langle a^{\dagger}_{\mathbf{k}\lambda}a_{\mathbf{k}-\mathbf{q},\lambda'}b_{\mathbf{q}j}\rangle - g^{\lambda\lambda' *}_{\mathbf{kq}j}\,\langle a^{\dagger}_{\mathbf{k}-\mathbf{q},\lambda'}a_{\mathbf{k}\lambda}b^{\dagger}_{\mathbf{q}j}\rangle\Big]. \tag{1.42}$$

The dynamics are driven by the phonon assisted polarisation $\langle a^{\dagger}_{\mathbf{k}\lambda}a_{\mathbf{k}-\mathbf{q},\lambda'}b_{\mathbf{q}j}\rangle$ and the corresponding equation of motion can be solved within the second-order Born-Markov approximation. Inserting the solution into the equations for the carrier occupation and the phonon number, we get

$$\dot{\rho}^{\lambda}_{\mathbf{k}}\big|_{H_{c,ph}} = \Gamma^{in(cp)}_{\mathbf{k}\lambda}\,(1-\rho^{\lambda}_{\mathbf{k}}) - \Gamma^{out(cp)}_{\mathbf{k}\lambda}\,\rho^{\lambda}_{\mathbf{k}} \tag{1.43}$$

$$\dot{n}^{j}_{\mathbf{q}} = \Gamma^{em}_{\mathbf{q}j}\,(n^{j}_{\mathbf{q}}+1) - \Gamma^{abs}_{\mathbf{q}j}\,n^{j}_{\mathbf{q}} - \gamma^{j}_{ph}\big(n^{j}_{\mathbf{q}} - n^{j}_{\mathbf{q},B}\big). \tag{1.44}$$

In the equation for the phonon number the experimental phonon lifetime $\gamma^{j}_{ph} = 1.2\,\mathrm{ps}^{-1}$ [54] is introduced, which describes the decay of the phonon number in the mode j towards the equilibrium Bose distribution $n^{j}_{\mathbf{q},B}$. The phonon induced in-scattering rate of carriers $\Gamma^{in(cp)}_{\mathbf{k}\lambda}$ and the phonon emission

rate $\Gamma^{em}_{\mathbf{q}j}$ are given by

$$\Gamma^{in(cp)}_{\mathbf{k}\lambda} = \frac{2\,\pi}{\hbar^2}\sum_{\mathbf{q}j}\sum_{\lambda'}\Big[|g^{\lambda'\lambda}_{\mathbf{k}+\mathbf{q},\mathbf{q}j}|^2\,\rho^{\lambda'}_{\mathbf{k}+\mathbf{q}}\big(n^j_{\mathbf{q}}+1\big)\,\delta\big(\omega_{\mathbf{k}+\mathbf{q},\lambda'}-\omega_{\mathbf{k}\lambda}-\omega_{\mathbf{q}j}\big), \\ + |g^{\lambda'\lambda}_{\mathbf{k}\mathbf{q}j}|^2\,\rho^{\lambda'}_{\mathbf{k}-\mathbf{q}}n^j_{\mathbf{q}}\,\delta\big(\omega_{\mathbf{k}-\mathbf{q},\lambda'}-\omega_{\mathbf{k}\lambda}+\omega_{\mathbf{q}j}\big)\Big] \tag{1.45}$$

$$\Gamma^{em}_{\mathbf{q}j} = \frac{2\,\pi}{\hbar^2}\sum_{\mathbf{k}\lambda\lambda'}|g^{\lambda'\lambda}_{\mathbf{k}\mathbf{q}j}|^2\,\rho^{\lambda}_{\mathbf{k}}(1-\rho^{\lambda'}_{\mathbf{k}-\mathbf{q}})\,\delta\big(\omega_{\mathbf{k}-\mathbf{q},\lambda'}-\omega_{\mathbf{k}\lambda}+\omega_{\mathbf{q}j}\big). \tag{1.46}$$

The time- and momentum-resolved scattering rate $\Gamma^{in(cp)}_{\mathbf{k}\lambda}$ describes processes where an electron with momentum $\mathbf{k}+\mathbf{q}$ scatters to a state with momentum $\mathbf{k}$ by emitting a phonon with momentum $\mathbf{q}$, the energy conservation is given by the delta function. Replacing $\rho^{\lambda}_{\mathbf{k}}$ by $(1-\rho^{\lambda}_{\mathbf{k}})$ and $n^j_{\mathbf{q}}$ by $(n^j_{\mathbf{q}}+1)$ in the in-scattering rate $\Gamma^{in(cp)}_{\mathbf{k}\lambda}$ as well as in the phonon emission rate $\Gamma^{em}_{\mathbf{q}j}$, the out-scattering rate $\Gamma^{out(cp)}_{\mathbf{k}\lambda}$ and the phonon absorption rate $\Gamma^{abs}_{\mathbf{q}j}$ can be obtained. The equation of motion for the microscopic polarisation can be derived in a similar way and reads

$$\dot{p}_{\mathbf{k}}\big|_{H_{c,ph}} = -\gamma^{(cp)}_{\mathbf{k}}p_{\mathbf{k}} + \sum_{\mathbf{k}'}U_{\mathbf{k}\mathbf{k}'}p_{\mathbf{k}'}, \tag{1.47}$$

$$\gamma^{(cp)}_{\mathbf{k}} = \frac{1}{2}\sum_{\lambda}\left(\Gamma^{in(cp)}_{\mathbf{k}\lambda}+\Gamma^{out(cp)}_{\mathbf{k}\lambda}\right), \tag{1.48}$$

with the diagonal dephasing $\gamma^{(cp)}_{\mathbf{k}}$. The off-diagonal dephasing $U_{\mathbf{k}\mathbf{k}'}$ will be neglected in the following.

Carrier-carrier scattering

The scattering equation for Coulomb induced processes can be derived by applying the correlation expansion and treating two-particle processes within the second-order Born-Markov approximation. The equation for the carrier-carrier scattering has the same form as the equation for the carrier-phonon

scattering

$$\dot{\rho}^{\lambda}_{\mathbf{k}}\big|_{H_{c,c}} = \Gamma^{in(cc)}_{\mathbf{k}\lambda}\,(1-\rho^{\lambda}_{\mathbf{k}}) - \Gamma^{out(cc)}_{\mathbf{k}\lambda}\,\rho^{\lambda}_{\mathbf{k}}, \tag{1.49}$$

$$\dot{p}_{\mathbf{k}}\big|_{H_{c,c}} = -\gamma^{(cc)}_{\mathbf{k}} p_{\mathbf{k}}, \tag{1.50}$$

with in-scattering rate $\Gamma^{in(cc)}_{\mathbf{k}\lambda}$ and diagonal dephasing $\gamma^{(cc)}_{\mathbf{k}}$ which are given by

$$\Gamma^{in(cc)}_{\mathbf{k}\lambda} = \frac{2\,\pi}{\hbar^2}\sum_{\mathbf{123}} V^{\mathbf{k}\lambda,\mathbf{1}}_{\mathbf{2,3}}\left[4\,V^{\mathbf{2,3}}_{\mathbf{k}\lambda,\mathbf{1}} - V^{\mathbf{3,2}}_{\mathbf{k}\lambda,\mathbf{1}}\right]\big(1-\rho_{\mathbf{1}}\big)\rho_{\mathbf{2}}\rho_{\mathbf{3}}\,\delta\big(\omega_{\mathbf{k}\lambda}+\omega_{\mathbf{1}}-\omega_{\mathbf{2}}-\omega_{\mathbf{3}}\big), \tag{1.51}$$

$$\gamma^{(cc)}_{\mathbf{k}} = \frac{1}{2}\sum_{\lambda}\left(\Gamma^{in(cc)}_{\mathbf{k}\lambda} + \Gamma^{out(cc)}_{\mathbf{k}\lambda}\right). \tag{1.52}$$

The out-scattering rate $\Gamma^{out(cc)}_{\mathbf{k}\lambda}$ can be obtained by replacing ρ with $\big(1-\rho\big)$. The coupling matrix element $V^{\mathbf{k}\lambda,\mathbf{1}}_{\mathbf{2,3}}\left[4\,V^{\mathbf{2,3}}_{\mathbf{k}\lambda,\mathbf{1}} - V^{\mathbf{3,2}}_{\mathbf{k}\lambda,\mathbf{1}}\right]$ consists of two parts, one for direct processes and the second one that describes exchange processes. The factor 4 takes the spin and valley degeneracies into account.

Carrier-light and carrier-field interaction

The interactions of carriers with light $H_{c,l}$, the coupling with an external electric field $H_{c,f}$ as well as the free carriers H_0 are described by a one-particle Hamilton operator. Therefore the equations of motion for the carrier occupation and polarisation do not couple to higher-order correlations and can be directly derived from the Heisenberg equations of motion

$$\dot{\rho}^{\lambda}_{\mathbf{k}}\big|_{H_0+H_{c,l}+H_{c,f}} = \pm 2\,\mathrm{Im}\big[\Omega^{vc,*}_{\mathbf{k}} p_{\mathbf{k}}\big] - \frac{e_0}{\hbar}\mathbf{E}\cdot\nabla_{\mathbf{k}}\rho^{\lambda}_{\mathbf{k}}, \tag{1.53}$$

$$\dot{p}_{\mathbf{k}}\big|_{H_0+H_{c,l}+H_{c,f}} = \frac{i}{\hbar}(\varepsilon^{v}_{\mathbf{k}} - \varepsilon^{c}_{\mathbf{k}}) - i\Omega^{vc}_{\mathbf{k}}\big(\rho^{e}_{\mathbf{k}}(\mathbf{r}) + \rho^{h}_{\mathbf{k}}(\mathbf{r}) - 1\big) - \frac{e_0}{\hbar}\mathbf{E}\cdot\nabla_{\mathbf{k}} p_{\mathbf{k}}, \tag{1.54}$$

with the Rabi frequency $\Omega^{vc}_{\mathbf{k}} = i\frac{e_0}{m_0}\mathbf{M}^{vc}_{\mathbf{k}}\cdot\mathbf{A}$. The "+(-)" sign stands for conduction (valence) band.

Diffusion

In the previous sections we derived the equations of motion for the electron/hole occupation probability $\rho^{\lambda}_{\mathbf{k}}$, the microscopic polarisation $p_{\mathbf{k}}$, and the phonon number $n^{j}_{\mathbf{q}}$ for a homogeneous system, this means with no spatial dependecies. In this section spatial effects are introduced by transforming the occupation probability into the Wigner formalism [55, 56]. We consider fluctuations of the occupation probability $\rho^{\tilde{\lambda}}_{\mathbf{k},\mathbf{q}} = \langle a^{\dagger}_{\mathbf{k}-\mathbf{q}/2,\lambda} a_{\mathbf{k}+\mathbf{q}/2,\lambda} \rangle$ and perform the Fourier transformation $\mathcal{F}_{\mathbf{q}}$ with respect to the momentum difference $\mathbf{q}$

$$f^{\lambda}_{\mathbf{k}}(\mathbf{r}) = \mathcal{F}_{\mathbf{q}}\big[\rho^{\lambda}_{\mathbf{k},\mathbf{q}}\big] = \sum_{\mathbf{q}} e^{i\mathbf{q}\mathbf{r}} \rho^{\lambda}_{\mathbf{k},\mathbf{q}}. \tag{1.55}$$

Note that the Wigner function $f^{\lambda}_{\mathbf{k}}(\mathbf{r})$ is a quasi-probability function, i.e. $f^{\lambda}_{\mathbf{k}}(\mathbf{r})$ can be negative. If this is the case, the negativity of the Wigner function can be used to detect non-classical behaviour, but not every quantum state implies a negative Wigner function, e.g. pure states provide non-negative Wigner functions. Nevertheless, integration over $\mathbf{r}$ or $\mathbf{k}$ gives the actual distribution in momentum space or the carrier density in real space, i.e.

$$\rho^{\lambda}_{\mathbf{k}} = \frac{1}{L^2} \int d\mathbf{r}\, f^{\lambda}_{\mathbf{k}}(\mathbf{r}), \tag{1.56}$$

$$n(\mathbf{r}) = \frac{1}{L^2} \sum_{\mathbf{k}\lambda} f^{\lambda}_{\mathbf{k}}(\mathbf{r}). \tag{1.57}$$

Next, we derive the equations of motion for the Wigner function. We start with the equation of motion for the carrier fluctuation $\rho^{\lambda}_{\mathbf{k},\mathbf{q}}$ for the free particle Hamilton operator H_0, which reads

$$i\hbar \dot{\rho}^{\lambda}_{\mathbf{k},\mathbf{q}} = \big(\varepsilon^{\lambda}_{\mathbf{k}+\mathbf{q}/2} - \varepsilon^{\lambda}_{\mathbf{k}-\mathbf{q}/2}\big)\rho^{\lambda}_{\mathbf{k},\mathbf{q}}. \tag{1.58}$$

The dynamics of the fluctuation is driven by the energy difference of initial and final state $\varepsilon^{\lambda}_{\mathbf{k}+\mathbf{q}/2} - \varepsilon^{\lambda}_{\mathbf{k}-\mathbf{q}/2}$. To determine the corresponding equation for the Wigner function we perform a Fourier transform according to equation (1.55)

$$i\hbar \dot{f}^{\lambda}_{\mathbf{k}}(\mathbf{r}) = i\hbar \mathcal{F}_{\mathbf{q}}\big[\dot{\rho}^{\lambda}_{\mathbf{k},\mathbf{q}}\big] = \mathcal{F}_{\mathbf{q}}\big[\big(\varepsilon^{\lambda}_{\mathbf{k}+\mathbf{q}/2} - \varepsilon^{\lambda}_{\mathbf{k}-\mathbf{q}/2}\big) \cdot \rho^{\lambda}_{\mathbf{k},\mathbf{q}}\big]. \tag{1.59}$$

The evaluation of the right hand side of the equation of motion is not straight forward since there is a product of two functions which implies a convolution (which we denote with $*$) of the electronic dispersion $\varepsilon^\lambda_{\mathbf{k}}$ with the fluctuation $\rho^\lambda_{\mathbf{k},\mathbf{q}}$, i.e. $\mathcal{F}_\mathbf{q}\big[\big(\varepsilon^\lambda_{\mathbf{k}+\mathbf{q}/2} - \varepsilon^\lambda_{\mathbf{k}-\mathbf{q}/2}\big)\cdot\rho^\lambda_{\mathbf{k},\mathbf{q}}\big] = \mathcal{F}_\mathbf{q}\big[\big(\varepsilon^\lambda_{\mathbf{k}+\mathbf{q}/2} - \varepsilon^\lambda_{\mathbf{k}-\mathbf{q}/2}\big)\big] * \mathcal{F}_\mathbf{q}\big[\rho^\lambda_{\mathbf{k},\mathbf{q}}\big]$.

The aim in the following is to approximate equation (1.59) in such a way that on the right hand side no integrals (or convolutions) occur. We start with applying the inverse Fourier transform for $\rho^\lambda_{\mathbf{k},\mathbf{q}} = \int d\mathbf{r}' e^{-i\mathbf{q}\mathbf{r}'} f^\lambda_\mathbf{k}(\mathbf{r}')$ which leads to

$$i\hbar \dot{f}^\lambda_\mathbf{k}(\mathbf{r}) = \int d\mathbf{r}' \sum_\mathbf{q} \left(\varepsilon^\lambda_{\mathbf{k}+\mathbf{q}/2} - \varepsilon^\lambda_{\mathbf{k}-\mathbf{q}/2}\right) e^{i\mathbf{q}\mathbf{r}'} f^\lambda_\mathbf{k}(\mathbf{r}-\mathbf{r}'), \tag{1.60}$$

where we already shifted the integration from $\mathbf{r}'$ to $\mathbf{r}-\mathbf{r}'$. To simplify this integro-differential equation we expand the Wigner function to the first order in $\mathbf{r}'$

$$f^\lambda_\mathbf{k}(\mathbf{r}-\mathbf{r}') \approx f^\lambda_\mathbf{k}(\mathbf{r}) - \mathbf{r}'\cdot\nabla_\mathbf{r} f^\lambda_\mathbf{k}(\mathbf{r}). \tag{1.61}$$

Next, we shift the momentum $\mathbf{q} \to \pm 2\,(\mathbf{q}-\mathbf{k})$ to get $\left(\varepsilon^\lambda_{\mathbf{k}+\mathbf{q}/2} - \varepsilon^\lambda_{\mathbf{k}-\mathbf{q}/2}\right) e^{i\mathbf{q}\mathbf{r}'} = \varepsilon_\mathbf{q}\left(e^{2\,i(\mathbf{q}-\mathbf{k})\mathbf{r}'} - e^{-2\,i(\mathbf{q}-\mathbf{k})\mathbf{r}'}\right)$. We use the identity $\mathbf{r}' e^{\pm 2\,i(\mathbf{q}-\mathbf{k})\mathbf{r}'} = \mp\frac{i}{2}\nabla_\mathbf{q} e^{\pm 2\,i(\mathbf{q}-\mathbf{k})\mathbf{r}'}$ and shift the $\mathbf{q}$-derivative to the electron dispersion via integration by parts. Now, the $\mathbf{r}'$-integral depends only on the exponential function which results into a delta function $\delta_{\mathbf{k},\mathbf{q}}$. Since the $\mathbf{q}$-derivative induces different signs on the two exponentials the first order of the Wigner function does not vanish (in contrast to the zeroth order).
Finally, the equation of motion for the Wigner function for the free Hamilton operator is given by

$$\dot{f}^\lambda_\mathbf{k}(\mathbf{r}) = -\frac{\nabla_\mathbf{k}\varepsilon^\lambda_\mathbf{k}}{\hbar}\cdot\nabla_\mathbf{r} f^\lambda_\mathbf{k}(\mathbf{r}). \tag{1.62}$$

To derive the equations of motion for the Wigner function, the polarisation and the phonon number with the full Hamilton operator we make the following assumptions. We assume that diffusion processes in the polarisation can be neglected, since the polarisation vanishes directly after the optical excitation. In contrast, the relaxation of carriers is on a picosecond timescale which is comparable to diffusion processes, and therefore the diffusion term can not be neglected in the equation for the Wigner function. We neglect also diffusion in the phonon number since the phonon diffusion is much slower than

the electronic diffusion, which is a consequence of the flat phonon dispersion. Additionally, scattering processes between different positions are not taken into account, since we expect them to be small compared to the diffusion. In summary, the previous equations of motion for $\rho_{\mathbf{k}}^{\lambda}$ remain unaltered when transforming the carrier occupation into the Wigner function.

Spatio-temporal Bloch equations

Using the Heisenberg equation of motion for the Wigner function, we derive the spatio-temporal graphene Bloch equations in second-order Born-Markov approximation for the carrier and phonon dynamics under the influence of an electric field and diffusion

$$\begin{aligned}\dot{f}_{\mathbf{k}}^{\lambda}(\mathbf{r},t) &= \Gamma_{\mathbf{k}\lambda}^{\mathrm{in}}(\mathbf{r},t)\left(1-f_{\mathbf{k}}^{\lambda}(\mathbf{r},t)\right) - \Gamma_{\mathbf{k}\lambda}^{\mathrm{out}}(\mathbf{r},t)\, f_{\mathbf{k}}^{\lambda}(\mathbf{r},t) \\ &\quad + 2\,\mathrm{Im}\left[\Omega_{\mathbf{k}}^{vc,*}(\mathbf{r},t) p_{\mathbf{k}}(\mathbf{r},t)\right] \\ &\quad - \frac{e_0}{\hbar}\mathbf{E}(\mathbf{r})\cdot\nabla_{\mathbf{k}} f_{\mathbf{k}}^{\lambda}(\mathbf{r},t) - \frac{\nabla_{\mathbf{k}}\varepsilon_{\mathbf{k}}^{\lambda}(\mathbf{r})}{\hbar}\cdot\nabla_{\mathbf{r}}\, f_{\mathbf{k}}^{\lambda}(\mathbf{r},t), \end{aligned} \tag{1.63}$$

$$\begin{aligned}\dot{p}_{\mathbf{k}}(\mathbf{r},t) &= i\Delta\omega_{\mathbf{k}}(\mathbf{r},t) p_{\mathbf{k}}(\mathbf{r},t) - i\Omega_{\mathbf{k}}^{vc}(\mathbf{r},t)\Big(f_{\mathbf{k}}^{e}(\mathbf{r},t) + f_{\mathbf{k}}^{h}(\mathbf{r},t) - 1\Big) \\ &\quad - \frac{e_0}{\hbar}\mathbf{E}(\mathbf{r})\cdot\nabla_{\mathbf{k}} p_{\mathbf{k}}(\mathbf{r},t), \end{aligned} \tag{1.64}$$

$$\begin{aligned}\dot{n}_{\mathbf{q}}^{j}(\mathbf{r},t) &= \Gamma_{\mathbf{q}j}^{\mathrm{em}}(\mathbf{r},t)\Big(n_{\mathbf{q}}^{j}(\mathbf{r},t)+1\Big) - \Gamma_{\mathbf{q}j}^{\mathrm{abs}}(\mathbf{r},t)\, n_{\mathbf{q}}^{j}(\mathbf{r},t) \\ &\quad - \gamma_{\mathrm{ph}}\Big(n_{\mathbf{q}}^{j}(\mathbf{r},t) - n_{\mathbf{q},\mathrm{B}}^{j}(\mathbf{r})\Big) \end{aligned} \tag{1.65}$$

with $\Delta\omega_{\mathbf{k}} = \frac{1}{\hbar}(\varepsilon_{\mathbf{k}}^{v} - \varepsilon_{\mathbf{k}}^{c} + i\gamma_{\mathbf{k}})$. This is a coupled system of differential equations for the carrier occupation $\rho_{\mathbf{k}}^{\lambda}$ for $\lambda = e,h$, the microscopic polarisation $p_{\mathbf{k}}$ and the phonon number $n_{\mathbf{q}}^{j}$ with dephasing $\gamma_{\mathbf{k}} = \gamma_{\mathbf{k}}^{cp} + \gamma_{\mathbf{k}}^{cc}$ and the in- and out-scattering rates $\Gamma_{\mathbf{k}\lambda}^{in/out} = \Gamma_{\mathbf{k}\lambda}^{in/out(cp)} + \Gamma_{\mathbf{k}\lambda}^{in/out(cc)}$. Note that in the equation for the phonon number no contributions of $H_{c,c}$, $H_{c,l}$ and $H_{c,f}$ appear. These contributions are neglected since they have only an impact on higher orders of the correlation expansion, which goes beyond the scope of this thesis. The equations describe the time- and momentum-resolved coupled dynamics of

electrons/holes, phonons, and the microscopic polarisation. The dynamics of electrons in the conduction band and holes in the valence band are symmetric, but have different initial conditions for doped graphene samples. In a homogeneous system the diffusion term vanishes and the Wigner function equals to the carrier occupation.

1.5 Electrical current

In this section we take a first look on how an electric field correspond to an electrical current in the case of a homogeneous system. First, we determine the current for graphene, and afterwards we introduce a moving coordinate frame to simplify the equations of motion.

Current

The current density in two-dimensional materials is defined as

$$\mathbf{j}(t) = -\frac{g\, e_0}{m_0 L^2} \sum_{if} \langle f|\mathbf{p} - e_0\mathbf{A}|i\rangle \langle a_f^+ a_i \,\rangle \tag{1.66}$$

with the area of the graphene sheet L^2, initial and final Bloch states i,f, the momentum $\mathbf{p} = -i\hbar\nabla_{\mathbf{r}}$ and the factor $g = 4$ accounts for spin and valley degeneracies. To study the transport properties in graphene only the intraband current has to be considered, applying furthermore a homogeneity assumption implies equal states i and f. The occuring quantity $\langle f|\nabla_{\mathbf{r}}|f\rangle$ can then be determined by solving the Schrödinger equation for the Bloch functions $|f\rangle = \varphi_{\mathbf{k}\lambda}(\mathbf{r})$

$$\left[-\frac{\hbar^2}{2\, m_0} + V(\mathbf{r}) \right] \varphi_{\mathbf{k}\lambda}(\mathbf{r}) = \varepsilon_{\mathbf{k}}^{\lambda} \varphi_{\mathbf{k}\lambda}(\mathbf{r}). \tag{1.67}$$

Using the definition of the Bloch function and multiplying the Schrödinger equation with $\varphi^*_{\mathbf{k}\lambda}(\mathbf{r})\nabla_{\mathbf{k}}$ yields $\langle f|\nabla_{\mathbf{r}}|f\rangle = \frac{im_0}{\hbar^2}\nabla_{\mathbf{k}}\varepsilon_{\mathbf{k}}^{\lambda}$ and for the intraband current density one has[42]:

$$\mathbf{j}(t) = -\frac{g\, e_0}{\hbar L^2} \sum_{\mathbf{k}\lambda} \rho_{\mathbf{k}}^{\lambda}(t) \nabla_{\mathbf{k}} \varepsilon_{\mathbf{k}}^{\lambda} = -\frac{g\, e_0 v_{\mathrm{F}}}{L^2} \sum_{\mathbf{k}\lambda} \rho_{\mathbf{k}}^{\lambda}(t)\, \mathbf{e}_{\mathbf{k}}. \tag{1.68}$$

In conventional materials, the electronic dispersion is parabolic, i.e. $\varepsilon_{\mathbf{k}}^{\lambda} = \hbar^2\mathbf{k}^2/(2\,m)$ and the current density is proportional to the momentum $\mathbf{k}$, such that the current diverges with time in the case without many-particle scattering. The linear band structure of graphene $\varepsilon_{\mathbf{k}}^{\lambda} = \hbar v_{\mathrm{F}}|\mathbf{k}|$ with the Fermi velocity v_{F} leads to a qualitatively different behaviour of the current density. The latter is now proportional to the unity vector $\nabla_{\mathbf{k}}|\mathbf{k}| = \mathbf{k}/|\mathbf{k}| = \mathbf{e}_{\mathbf{k}}$. As a result, the current is not affected by the magnitude of the momentum but solely by its direction and thus in contrast to conventional materials the generation and decay of the current density can be influenced by both carrier-phonon and carrier-carrier scattering [57].

Shift of carriers

Now, we solve the equation for the field term which is given by

$$\dot{\rho}_{\mathbf{k}}^{\lambda}(t) = -\frac{e_0}{\hbar}\mathbf{E}\cdot\nabla_{\mathbf{k}}\rho_{\mathbf{k}}^{\lambda}(t). \tag{1.69}$$

This equation can be solved by using the Ansatz $\rho_{\mathbf{k}}^{\lambda}(t) = g^{\lambda}(\mathbf{k} - \frac{e_0}{\hbar}\mathbf{E}t)$ for any function g, e.g. a Fermi distribution. This means that an electric field shifts carriers in momentum space. The resulting current is given by

$$\mathbf{j}(t) = -\frac{g\,e_0 v_{\mathrm{F}}}{L^2}\sum_{\mathbf{k}\lambda} g^{\lambda}\big(\mathbf{k} - \frac{e_0}{\hbar}\mathbf{E}t\big)\,\mathbf{e}_{\mathbf{k}}. \tag{1.70}$$

Note that the amplitude of the current is determined by the asymmetry of the shifted distribution $g^{\lambda}(\mathbf{k} - \frac{e_0}{\hbar}\mathbf{E}t)$. The influence of the electric field on the carrier dynamics will be discussed in more detail in chapter 3.

It is possible to transform the spatio-temporal Bloch equations in such a way that the terms with the electric field vanishes by using the coordinate transformation $\mathbf{k} \to \mathbf{k} - \frac{e_0}{\hbar}\mathbf{E}t$, which correspond to the transformation of the system into a moving reference frame [58]. The time derivative is transformed by $\frac{d}{dt} \to \frac{d}{dt} - \frac{e_0}{\hbar}\mathbf{E}\cdot\nabla_{\mathbf{k}}$, such that the field term is canceled. The resulting equations correspond to the standard graphene Bloch equations without electric field, where the field induced dynamics are hidden in the motion of the coordinates. Note that if impurities are taken into account these impurities start moving in the new reference frame.

To understand the transformation in more detail, we solve exemplary the equation for the carrier density in the transformed coordinates, which is given by $\dot{\rho}^{\lambda}_{\mathbf{k}-\frac{e_0}{\hbar}\mathbf{E}t}(t) = h^{\lambda}_{\mathbf{k}-\frac{e_0}{\hbar}\mathbf{E}t}(t)$ where h denotes the right hand side of equation (1.63). The time derivative can be approximated by the differential quotient, i.e. $\dot{\rho}^{\lambda}_{\mathbf{k}-\frac{e_0}{\hbar}\mathbf{E}t}(t) = (\rho^{\lambda}_{\mathbf{k}-\frac{e_0}{\hbar}\mathbf{E}(t+dt)}(t+dt) - \rho^{\lambda}_{\mathbf{k}-\frac{e_0}{\hbar}\mathbf{E}t}(t))/dt = h^{\lambda}_{\mathbf{k}-\frac{e_0}{\hbar}\mathbf{E}t}(t)$. Now, we shift the momentum coordinate back to the original non-moving frame which results into

$$\rho^{\lambda}_{\mathbf{k}-\frac{e_0}{\hbar}\mathbf{E}dt}(t+dt) = \rho^{\lambda}_{\mathbf{k}}(t) + h^{\lambda}_{\mathbf{k}}(t)\,dt. \tag{1.71}$$

This equation demonstrates that applying an electric field induces a shift of $\rho^{\lambda}_{\mathbf{k}}$ in $\mathbf{k}$-space (the same holds for $p_{\mathbf{k}}$).

1.6 Analytic evaluation of diffusion

In this section we discuss the diffusion term analytically to get first insights on the influence of the diffusion to the carrier dynamics. The diffusion term reads

$$\dot{f}^{\lambda}_{\mathbf{k}}(\mathbf{r},t) = -\frac{1}{\hbar}\nabla_{\mathbf{k}}\varepsilon^{\lambda}_{\mathbf{k}} \cdot \nabla_{\mathbf{r}} f^{\lambda}_{\mathbf{k}}(\mathbf{r},t). \tag{1.72}$$

In the following we consider electrons in the conduction band and suppress the index λ (we get the same results for holes in the valence band). First, we show that the diffusion term induces a current, which can be related to the continuity equation. Afterwards, we find an expression for the corresponding diffusion field (in analogy to an electric field) and discuss the occuring effects on the current. In the last part we present analytic expressions for the conductivity and the Seebeck coefficient.

Continuity equation

We start with the integration over the carrier momentum $\mathbf{k}$. The integration of the left hand side of equation (1.72) is the time derivative of the charge carrier density $n(\mathbf{r},t)$ which is defined as $n(\mathbf{r},t) = -e_0\frac{g}{L^2}\sum_{\mathbf{k}} f_{\mathbf{k}}(\mathbf{r},t)$. The right hand side can be rewritten such that the spatial derivative acts on

the whole expression as divergence, i.e. $-\frac{-ge_0}{\hbar L^2}\sum_{\mathbf{k}}\nabla_{\mathbf{k}}\varepsilon_{\mathbf{k}}\cdot\nabla_{\mathbf{r}}f^{\lambda}_{\mathbf{k}}(\mathbf{r},t)=-\nabla_{\mathbf{r}}\cdot\big(-\frac{ge_0}{\hbar L^2}\sum_{\mathbf{k}}\nabla_{\mathbf{k}}\varepsilon^{\lambda}_{\mathbf{k}}f^{\lambda}_{\mathbf{k}}(\mathbf{r},t)\big)=-\mathrm{div}\,\mathbf{j}(\mathbf{r},t)$, where we used the definition of the charge current $\mathbf{j}(\mathbf{r},t)$. Finally, the integration of the diffusion term gives the continuity equation[59]

$$\dot{n}(\mathbf{r},t)=-\mathrm{div}\,\mathbf{j}(\mathbf{r},t). \tag{1.73}$$

The continuity equation describes that a change of the local charge density corresponds to the generation of a local charge current, reflecting the conservation of charge.

Current

According to the continuity equation the diffusion changes the local carrier density and induces local currents. To understand the generation of currents we assume that the carrier distribution can be described as Fermi distribution, i.e.

$$f_{\mathbf{k}}(\mathbf{r},t)=f_{\mathbf{k}}\big(\mu(\mathbf{r},t),T(\mathbf{r},t)\big)\big)=\big(e^{(\varepsilon_{\mathbf{k}}-\mu(\mathbf{r},t))/k_BT(\mathbf{r},t)}+1\big)^{-1} \tag{1.74}$$

where we assumed that doping $\mu(\mathbf{r})$ and temperature $T(\mathbf{r})$ depend on the spatial position $\mathbf{r}$ and time t. With these specific dependencies of the carrier distribution the spatial derivative can be rewritten as

$$\dot{f}_{\mathbf{k}}(\mathbf{r},t)=-\frac{1}{\hbar}\frac{\partial\varepsilon_{\mathbf{k}}}{\partial\mathbf{k}}\frac{\partial f_{\mathbf{k}}}{\partial\mathbf{r}}=-\frac{1}{\hbar}\frac{\partial\varepsilon_{\mathbf{k}}}{\partial\mathbf{k}}\left(\frac{\partial f_{\mathbf{k}}}{\partial\mu}\frac{\partial\mu}{\partial\mathbf{r}}+\frac{\partial f_{\mathbf{k}}}{\partial T}\frac{\partial T}{\partial\mathbf{r}}\right). \tag{1.75}$$

The temperature derivative in the second term can be transformed into a doping derivative, i.e. $\partial f_{\mathbf{k}}/\partial T=(\varepsilon_{\mathbf{k}}-\mu)/T\,\partial f_{\mathbf{k}}/\partial\mu$ and we get

$$\dot{f}_{\mathbf{k}}(\mathbf{r},t)=-\frac{1}{\hbar}\left(\frac{\partial\mu}{\partial\mathbf{r}}+\frac{\varepsilon_{\mathbf{k}}-\mu}{T}\frac{\partial T}{\partial\mathbf{r}}\right)\frac{\partial\varepsilon_{\mathbf{k}}}{\partial\mathbf{k}}\frac{\partial f_{\mathbf{k}}}{\partial\mu}. \tag{1.76}$$

Now, we introduce a $\mathbf{k}$ derivative of the carrier distribution via $\partial f_{\mathbf{k}}/\partial\mathbf{k}=-\partial\varepsilon_{\mathbf{k}}/\partial\mathbf{k}\,\partial f_{\mathbf{k}}/\partial\mu$ which results into

$$\dot{f}_{\mathbf{k}}(\mathbf{r},t)=\frac{1}{\hbar}\left(\nabla_{\mathbf{r}}\mu(\mathbf{r},t)+\frac{\varepsilon_{\mathbf{k}}-\mu(\mathbf{r},t)}{T(\mathbf{r},t)}\nabla_{\mathbf{r}}T(\mathbf{r},t)\right)\cdot\nabla_{\mathbf{k}}f_{\mathbf{k}}(\mathbf{r},t). \tag{1.77}$$

By defining the diffusion field $\mathbf{E}_{\mathbf{k}}^{\text{diff}} = \frac{1}{e_0}\nabla_{\mathbf{r}}\mu + \frac{\varepsilon_{\mathbf{k}}-\mu}{e_0 T}\nabla_{\mathbf{r}}T$ the equation looks the same as the term for an external field, cf. equation (1.69). The first term describes the photovoltaic effect and the second term denotes the thermoelectric effect.
For example, local optical excitation of carriers lead to local heating which correspond to temperature gradients and result into a diffusion current. Note that in a homogeneous system the total diffusion current is zero, since carriers diffuse into all directions.
In a p-n junction the gradient of doping between p- and n-region leads to diffusion of electrons from n to p. Since the diffusion of electrons is favourable from n to p the total diffusion current is non-zero. To reach a equilibrium situation we have to take into account that diffusion of electrons from n to p (and diffusion of holes from p to n) build up a depletion zone, where the opposite charge of electrons and holes induces an electric field which counter acts the diffusion field. Optically induced heating of a p-n junction leads to a non-vanishing total current via the Seebeck effect, note that the diffusion field scales with doping and temperature gradient.

Conductivity and Seebeck coefficient

Now, we solve the diffusion term in the relaxation time approximation and determine the corresponding current. We assume that the carrier occupation can be written as a sum of an unperturbated Fermi distribution $\rho_{\mathbf{k}}^{\lambda(0)}$ and a small perturbation $\rho_{\mathbf{k}}^{\lambda(1)}$, i.e. $\rho_{\mathbf{k}}^{\lambda} \approx \rho_{\mathbf{k}}^{\lambda(0)} + \rho_{\mathbf{k}}^{\lambda(1)}$. Furthermore, we assume that the perturbation relaxes into the equilibrium with relaxation time $\tau_{\mathbf{k}}$. Taking this into account we add a term $-\frac{1}{\tau_{\mathbf{k}}}\rho_{\mathbf{k}}^{\lambda(1)}$ and the diffusion term then reads

$$\dot{\rho}_{\mathbf{k}}^{\lambda} = \dot{\rho}_{\mathbf{k}}^{\lambda(0)} + \dot{\rho}_{\mathbf{k}}^{\lambda(1)} = \frac{e_0}{\hbar}\mathbf{E}_{\mathbf{k}}^{\text{diff}}\left(\frac{\partial \rho_{\mathbf{k}}^{\lambda(0)}}{\partial \mathbf{k}} + \frac{\partial \rho_{\mathbf{k}}^{\lambda(1)}}{\partial \mathbf{k}}\right) - \frac{1}{\tau_{\mathbf{k}}}\rho_{\mathbf{k}}^{\lambda(1)} \tag{1.78}$$

with $\alpha_{\mathbf{k}}$ being the prefactor in equation (1.77). The time derivative of the Fermi distribution $\dot{\rho}_{\mathbf{k}}^{\lambda(0)}$ vanishes, since this is already the equilibrium distribution and the momentum derivative $\partial\rho_{\mathbf{k}}^{\lambda(1)}/\partial\mathbf{k}$ will be neglected because it describes higher order effects. The remaining ordinary differential equation

can be directly solved

$$\rho_{\mathbf{k}}^{\lambda(1)} = \int_0^t dt' e^{-(t-t')/\tau_{\mathbf{k}}} \frac{e_0}{\hbar} \mathbf{E}_{\mathbf{k}}^{\text{diff}} \frac{\partial \rho_{\mathbf{k}}^{\lambda(0)}}{\partial \mathbf{k}} = \frac{e_0}{\hbar} \mathbf{E}_{\mathbf{k}}^{\text{diff}} \tau_{\mathbf{k}} \frac{\partial \rho_{\mathbf{k}}^{\lambda(0)}}{\partial \mathbf{k}} \left(1 - e^{-t/\tau_{\mathbf{k}}}\right). \quad (1.79)$$

In the regime where scattering is important, i.e. $t \gg \tau_{\mathbf{k}}$, the exponential vanishes and the solution simplifies. Now, we determine the corresponding current which reads

$$\mathbf{j} = -\frac{g e_0 v_{\text{F}}}{L^2} \sum_{\mathbf{k}\lambda} \rho_{\mathbf{k}}^{\lambda} \, \mathbf{e}_{\mathbf{k}} = -\frac{g e_0 v_{\text{F}}}{L^2} \sum_{\mathbf{k}\lambda} \left(\rho_{\mathbf{k}}^{\lambda(0)} + \rho_{\mathbf{k}}^{\lambda(1)} \right) \mathbf{e}_{\mathbf{k}}. \quad (1.80)$$

In equilibrium there is no current and the term going with $\rho_{\mathbf{k}}^{\lambda(0)}$ vanishes, since the sum over an symmetric function $\rho_{\mathbf{k}}^{\lambda(0)}$ times an asymmetric function $\mathbf{e}_{\mathbf{k}}$ is equal to zero. The remaining current is given by

$$\mathbf{j} = -\frac{g e_0^2 v_{\text{F}}}{\hbar L^2} \sum_{\mathbf{k}\lambda} \mathbf{E}_{\mathbf{k}}^{\text{diff}} \tau_{\mathbf{k}} \frac{\partial \rho_{\mathbf{k}}^{\lambda(0)}}{\partial \mathbf{k}} \, \mathbf{e}_{\mathbf{k}} = -\frac{g e_0^2 v_{\text{F}}^2}{L^2} \sum_{\mathbf{k}\lambda} \mathbf{E}_{\mathbf{k}}^{\text{diff}} \tau_{\mathbf{k}} \frac{\partial \rho_{\mathbf{k}}^{\lambda(0)}}{\partial \varepsilon_{\mathbf{k}}^{\lambda}}, \quad (1.81)$$

where we used $\partial \rho_{\mathbf{k}}^{\lambda(0)} / \partial \mathbf{k} = \partial \rho_{\mathbf{k}}^{\lambda(0)} / \partial \varepsilon_{\mathbf{k}}^{\lambda} \; \partial \varepsilon_{\mathbf{k}}^{\lambda} / \partial \mathbf{k}$ with $\partial \varepsilon_{\mathbf{k}}^{\lambda} / \partial \mathbf{k} = \hbar v_{\text{F}} \mathbf{e}_{\mathbf{k}}$ in the last step.
Finally, we plug in the definition of $\mathbf{E}_{\mathbf{k}}^{\text{diff}}$ and the current reads

$$\mathbf{j} = \sigma \mathbf{E} + S\sigma \, \nabla_{\mathbf{r}} T \quad (1.82)$$

with $\mathbf{E} = \nabla_{\mathbf{r}} \mu / e_0$, conductivity σ and Seebeck coefficient S, the latter two are defined as

$$\sigma = -\frac{g e_0^2 v_{\text{F}}^2}{L^2} \sum_{\mathbf{k}\lambda} \tau_{\mathbf{k}} \frac{\partial \rho_{\mathbf{k}}^{\lambda(0)}}{\partial \varepsilon_{\mathbf{k}}^{\lambda}} \quad (1.83)$$

$$S = -\frac{1}{\sigma} \frac{g e_0^2 v_{\text{F}}^2}{L^2} \sum_{\mathbf{k}\lambda} \tau_{\mathbf{k}} \frac{\varepsilon_{\mathbf{k}}^{\lambda} - \mu}{e_0 \, T} \frac{\partial \rho_{\mathbf{k}}^{\lambda(0)}}{\partial \varepsilon_{\mathbf{k}}^{\lambda}}. \quad (1.84)$$

The first term in equation (1.82) describes Ohm's law and the second term represents the thermoelectric current stemming from the Seebeck effect.

CHAPTER 2

Carrier dynamics in graphene

The focus in this chapter lies on the carrier dynamics in graphene without an external electric field in order to understand the main mechanisms for the relaxation of optically excited carriers[37, 39, 57, 60–63]. We use the solution of the graphene Bloch-equations to get full microscopic access to the time- and momentum resolved dynamics of coupled carriers and phonons. The Bloch-equations have been used successfully to model other low dimensional material like carbon nanotubes (CNTs)[64, 65] and transition metal dichalcogenides (TMDs)[66–68]. The treatment of all considered interactions on the same microscopic level allows the explanation of experimentally accessible effects as well as for the suggestion of new phenomena. The chapter is structured as followed: after introducing the possible scattering mechanisms the general relaxation processes are discussed. In the last section some results (publications V-XII) are presented.

2.1 Characterization of scattering channels

Coulomb scattering

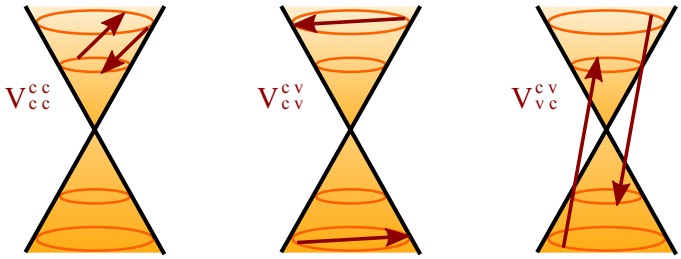

Figure 2.1: *Examples of non-Auger scattering channels, the first two processes show intraband scattering while the last one is a carrier-carrier interband process.*

Coulomb scattering is a two particle process, whose strength is determined by the matrix element $V^{\mathbf{12}}_{\mathbf{34}}$ containing $2^4 = 16$ different scattering channels. In the linear approximation of the band structure the velocity of carriers is the same in both bands and $\varepsilon^c_{\mathbf{k}}$ is equal to $-\varepsilon^v_{\mathbf{k}}$. In undoped graphene the electron-hole symmetry reduces the possible scattering channels by a factor of two. The transition where both carriers starts in the same band and both scatter to the other band is energetically forbidden, corresponding to $V^{\mathbf{k}_1 c, \mathbf{k}_2 c}_{\mathbf{k}_3 v, \mathbf{k}_4 v}$. The remaining seven scattering channels can be divided into two classes: Auger processes (4 channels) and non-Auger processes (3 channels). Both types include interband processes and the latter includes also intraband scattering. The non-Auger intra- and interband processes are illustrated in Fig. 2.1. Note that carrier-carrier processes with small transfer momentum are most efficient due to the $1/q^{13}$ (cf. eq. (1.28)) dependence of the Coulomb matrix element. Direct backscattering for intraband processes is forbidden but for interband processes it is very effective, such that the strongest Auger processes are on one line through the Dirac point.

Auger scattering and carrier multiplication

The linear band structure and the vanishing band gap in graphene enable efficient Auger scattering. In these Auger processes carriers scatter in such

a way that the number of carriers in one band changes and they can be divided into two subprocesses, namely Auger recombination (AR) and impact excitation (IE). For AR one carrier scatters from the conduction band to the valence band whereas the second carrier remains in the same band. IE is the corresponding inverse process. In conventional materials with parabolic band structure Auger processes are strongly suppressed since the fullfilling of momentum and energy conservation is unlikely in such systems. The main advantage of Auger scattering is that impact excitation generates additional carriers in the conduction band. This effect becomes important under optical excitation since one excited carrier excites other carriers via IE, resulting into a carrier multiplication (CM) and a larger carrier density. The carrier multiplication is quantified as the ratio $\mathrm{CM}(t) = \frac{n(t)-n_0}{n_{\mathrm{opt}}(t)}$ with the stationary carrier density before the optical excitation n_0, the pure optically-induced carrier density $n_{\mathrm{opt}}(t)$, and the total carrier density $n(t)$ containing the optical excitation as well as all scattering processes. CM takes place, i.e. $\mathrm{CM} > 1$, when the impact excitation exceeds the inverse process of Auger recombination resulting in an increased carrier density.

Carrier-phonon scattering

Similar to the carrier-carrier scattering, the carrier-phonon processes can be distinguished into intra- and interband scattering. A measure to divide these processes is the size of the phonon momentum q compared to the Dirac cone. For zero momentum the carrier-phonon scattering is vertical between valenceband and conductionband and is therefore an interband process, this process is only possible if the energetic distance between the two bands equal the discrete phonon energy. All momenta in the range $0 < q < \frac{\omega_q^j}{v_F}$ fullfill the condition for interband processes, such that one carrier in one band at a given momentum and angle are able to scatter to all other possible angles in the other band. Carrier-phonon scattering with $q = \frac{\omega_q^j}{v_F}$ is named parallel scattering, since the corresponding scattering processes are along the Dirac cone and can be both intra- and interband scattering. Carriers scattering with phonons with larger momenta remain in one band, i.e. the scattering channel is flatter than the dispersion of the band structure, this process is called intraband scattering. The involved phonons can be either absorbed or emitted in the scattering process, which correspond to an energy transfer

between the phononic system and the electronic system, e.g. carriers loose energy when they scatter in a phonon-emission process.

The angular dependence of the different phonon modes (Γ-*LO*, Γ-*TO*, Γ-*LA* and *K*-*TO*) is shown in Fig. 2.2. This is a view on top of the Dirac cone, which means that circles centered around the Dirac point (at zero momentum) describes the same energies but different angles. At the position of the red area a non-equilibrium density is set, which decreases due to carrier-phonon scattering, i.e. the difference of the carrier occupation becomes negative (red), and the out-scattered carriers form parts of an (orange) circle at lower energies. For interband scattering the dependence of the optical modes on the orange circle is inverted, the acoustic mode allows no interband transition since the dispersion of Γ-*LA* is much flatter than the electronic dispersion. The optical Γ modes complements each other resulting

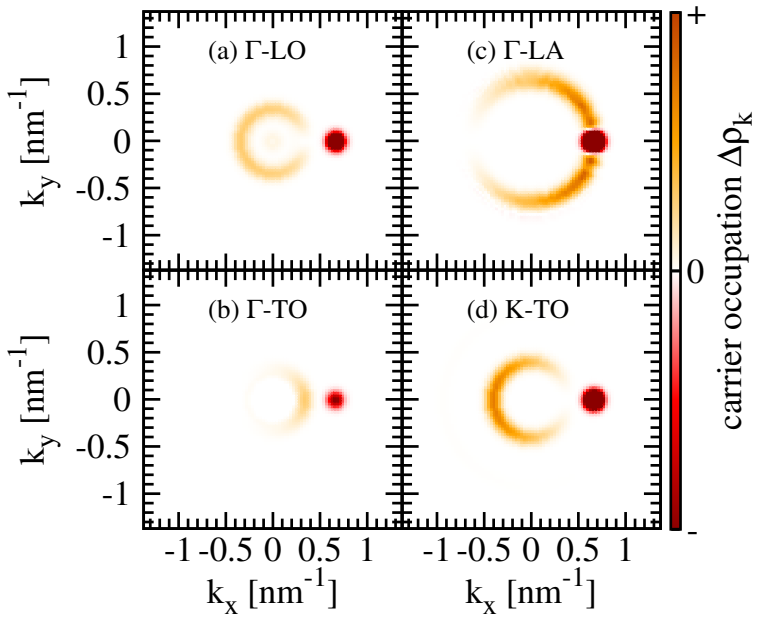

Figure 2.2: *Angular dependence of (a)* Γ-*LO, (b)* Γ-*TO, (c)* Γ-*LA and K*-*TO phonon modes for intraband scattering. The out scattering from the initial carrier density (red) induces the redistribution of carriers into the orange regions. The carrier occupation is shown around the Dirac point.*

into angular and energy relaxation in steps of the phonon energy. The K-TO mode describes the scattering between different Dirac valleys and favors backscattering (if mapped to one valley). The acoustic phonons Γ-LA induce forward scattering, in which the scattering strength scales with the phonon momentum q. In contrast to the optical modes the acoustic mode provides no significant energy relaxation, again due to the flat phonon dispersion, but allows momentum relaxation and continous energy transitions [39, 69].

2.2 Optical excitation and relaxation

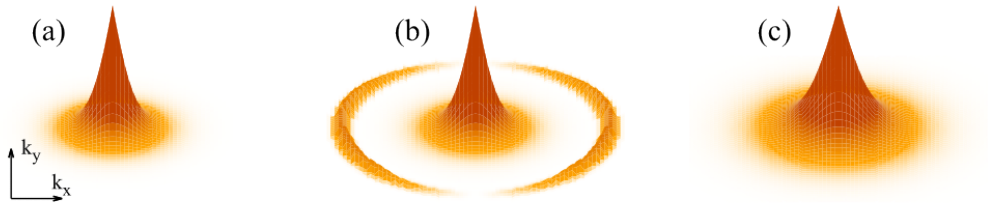

Figure 2.3: *(a) The thermal Fermi distribution at room temperature is optically excited (b), after a few tens of femtoseconds the anisotropy vanishes and the distribution thermalizes via carrier-carrier scattering, resulting into a hot Fermi distribution (c). Afterwards carrier-phonon processes lead to a cooling of carriers on a picosecond timescale.*

In this section the relaxation of carriers after an optical pulse excitation is studied. The optical field is defined via the vector potential $\mathbf{A}(t)$, which in the following is assumed to have a Gaussian shape

$$\mathbf{A}(t) = A_0 \hat{\mathbf{e}}_p \cos(\omega_L t) e^{-\frac{t^2}{2\sigma_t^2}}, \tag{2.1}$$

with the amplitude of the field A_0, the polarisation unity vector $\hat{\mathbf{e}}_p$, the frequency of the light ω_L and the pulse width σ_t. The strength of the excitation is given by the pump fluence E_{pf} which can be determined from the intensity of the light field. The pump fluence is given by

$$E_{pf} = A_0^2 \omega_L^2 \sigma_t \varepsilon_0 \sqrt{\pi} c/2 \tag{2.2}$$

with the velocity of light c. The angular dependence of the optical excitation correspond to the scalar product $|\mathbf{M}_{\mathbf{k}}^{vc} \cdot \hat{\mathbf{e}}_p|^2$ which follows a sinus of the angle between electron momentum and polarisation and provides therefore an anisotropic distribution of excited carriers. This behaviour is shown in Fig. 2.3 (b) for y-polarised light.

After the optical excitation, carriers relax on a timescale of hundreds of femtoseconds with respect to energy and momentum, i.e. the carriers form again a Fermi distribution but with higher temperature. Thereafter the electronic system equilibrate with the lattice on a picosecond timescale. The temperature of the hot Fermi distribution can be estimated if we assume that the whole absorbed energy of the optical pulse is transferred to the hot Fermi distribution, i.e. the energy loss to the lattice is negligible until the hot Fermi distribution is formed. Note, that a graphene sheet absorbs 2% of the incident light.

The carrier density n and the total carrier energy ε for a Fermi distribution with initial temperature T_0 can be determined by using $\int_0^\infty dx\, x^j/(e^x+1) = (1-2^{-j})\Gamma[j+1]\zeta[j+1]$ and are given by $n = k_B^2\pi/(3\hbar^2 v_F^2)\, T_0^2 = c_1 T_0^2$ and $\varepsilon = 6k_B^3\zeta(3)/(\hbar^2 v_F^2\pi)\, T_0^3 = c_2 T_0^3$. Using theses formulas, the carrier density can be expressed in terms of the energy $n = c_1(\varepsilon/c_2)^{2/3}$. Adding the energy of the optical pulse ε_{opt} to the carrier energy results in $n = c_1(T_0^3 + \varepsilon_{opt}/c_2)^{2/3}$ and the final temperature is given by

$$T = (T_0^3 + \varepsilon_{opt}/c_2)^{1/3} \tag{2.3}$$

the corresponding temperature increase is $\Delta T = T - T_0$. If ε_{opt}/c_2 is large compared to T_0 the temperature increase simplifies to $\Delta T = (\varepsilon_{opt}/c_2)^{1/3} - T_0$ and decays linearly with respect to the initial temperature.

Carrier-phonon relaxation

Consider first the case with pure carrier-phonon scattering. After the optical excitation carriers scatter in discrete energy steps towards the Dirac point. Note that the occupation of carriers increases with each lower energy level since the density of states decreases, assuming a constant carrier density. Recombination takes place when carriers are scattered to the energies of the phonon transition. With only optical phonon modes no thermalization

is possible, again due to the discrete energy steps. Taking carrier-phonon scattering with acoustic phonons into account, the carriers relax to a Fermi distribution on a timescale of hundreds of picoseconds. Due to the angular dependence of the scattering with all phonon modes the optical induced anisotropy is quickly reduced.

Carrier-carrier relaxation

The impact of carrier-carrier scattering on relaxation can be divided into several mechanisms: intraband scattering which leads to a broadening of the excited carriers, since if one carrier scatters towards lower energies a second carrier has to scatter to higher energies fulfilling energy- and momentum conservation. The impact excitation correspond to an accumulation of carriers near the Dirac point, due to the generation of carriers at the Dirac point and the scattering of the second assisted carrier to smaller energies. Auger recombination behaves in the opposite way, this means that the carrier occupation depopulates for small energies while the optically excited carriers scatter to higher energies. Note that Coulomb scattering is most efficient for collinear processes such that the angle relaxation is slow.

Full dynamics

Taking carrier-phonon as well as carrier-carrier scattering into account the relaxation dynamics can be completely described: The initial Fermi distribution is excited by an optical pulse establishing an anisotropy at the excitation energy, cf. Fig. 2.3(b). The carrier-carrier scattering leads to a thermalization on a 100 fs timescale, i.e. the excited carriers reach a quasi-equilibrium and form a hot Fermi distribution, cf. Fig. 2.3(c). The further relaxation is governed by carrier-phonon processes, which cool down the carrier distribution on a picosecond time scale, until the carrier distribution is in equilibrium with the phonon bath.

2.3 Results

In this section, a brief summary of the main results from the attached papers V-XI investigating the carrier dynamics in graphene will be provided.

Population inversion and graphene-based lasers

The scattering towards the Dirac point while the density of states is shrinking results in carrier occupations above one half for small energies. Such occupations are called population inversion, since for these carriers is the occupation in the conduction band higher than in the valence band. Such a broad population inversion was already measured [70, 71], and theoretically described [72, 73] and is a crucial ingredient to create a laser. A disadvantage in graphene is that non-radiative carrier recombination is very efficient such that the population inversion is destroyed after few femtoseconds. The strategy to achieve a long-lived population inversion, which enables optical gain and lasing, is to reduce the non-radiative recombination and enhance the carrier-photon coupling, cf. paper VI. The non-radiative scattering processes can be reduced by applying high-dielectric substrates which screen the carrier-carrier scattering. Another important aspect is the coupling of carriers to photons, which can be strengthen by using a high quality photonic crystal nanocavity. Such structures provide high quality factors such that the photonic losses are reduced. The statistics of the outcoming light reveals that for large dielectric constants, high quality factors and long pump pulses lasing can be achieved. In the presence of a magnetic field lasing can be achieved between different Landau levels [74, 75].

Tuning of recombination channels

The dynamics can be tuned to be dominated by either carrier-carrier or carrier-phonon scattering by applying different dielectric constants or excitation strengths, cf. paper V. The recombination by phonon-interband processes outperform the Auger induced recombination for large dielectric constants, due to strong screening of the Coulomb interaction. Another possibility for phonon dominated recombination is to weakly excite graphene

such that the optically generated carrier occupation and therefore the number of scattering partners is small. This suppresses the Coulomb scattering since it is a two particle process, in contrast to phonon scattering where only one electron is involved.

Double saturation

The carrier occupation generated by optical pumping, which correspond to the absorption, saturates for high pump fluences ($\approx 10\,\mathrm{mJ\ cm^{-2}}$) due to Pauli blocking. Additionally, graphene shows an unconventional second saturation at small fluences, which is three orders of magnitude smaller ($\approx 10\,\mu\mathrm{J\ cm^{-2}}$) and is governed by many-particle scattering processes, cf. paper VIII. The saturation for low fluences can be traced back to the efficient Coulomb induced out-scattering which depopulates the carriers at the excitation energy (the in-scattering is negligible in this regime). The rise of the out-scattering with the pump fluence is faster than the generation of carriers, such that the carrier occupation saturates.

Optical saturation at low energies

For low energies the optical dipol moment diverges, such that the excitation of carriers becomes faster than relaxation processes, which results into optical saturation, cf. paper VII. If the optical response is treated pertubatively, the saturated low energy states have to be excluded. Since more carrier states are saturated for stronger fields, the nonlinear response coefficients calculated with perturbation theory become field dependent.

Auger signatures

Carrier-phonon scattering can be suppressed by applying small temperatures or optical pumping with excitation energies below the phonon energies. These low excitation energies forbid scattering with optical phonons and small temperatures weaken the scattering with acoustic phonons. As result, a Auger dominated carrier dynamic is obtained, cf. paper XI. In the regime of low flu-

ences the impact excitation dominates, since carriers scatter towards lower energies and at the same time they excite additionally carriers, resulting into an accumulation of carriers in the vicinity of the Dirac point. For high fluences the dynamic is completely different, since many more carriers are excited and provide therefore more scattering partners. Intraband Coulomb scattering leads to a broadening of the excited carriers and, in contrast to the low fluence regime, carriers are scattered above the excitation energy. Due to efficient Auger recombination a pronounced loss of carriers can be observed at the Dirac point.

Anisotropy

The optical excitation of graphene is anisotropic in k-space, cf. Fig. 2.3. The many-particle scattering reduces the asymmetry on a timescale of tens of femtoseconds due to carrier-phonon scattering. The reduction can be manipulated with different substrates, fluences and dopings, cf. paper X. At low fluences the asymmetry decays fast since carrier-phonon scattering across the Dirac cone is very efficient. For high fluences the carrier occupation at the excitation energy is also enhanced. The Coulomb scattering, which is a two-particle process and therefore becomes more effective for increased carrier occupations, induces fast energy relaxation. The scattering of carriers to the vicinity of the Dirac point is faster than the phonon-induced reduction of the asymmetry, such that an asymmetric carrier distribution below the phonon energy, where the relaxation via carrier-phonon scattering is suppressed, can be established. Subsequently, the anisotropy is reduced by non-colinear Coulomb processes on a larger timescale. Another way to enlarge the lifetime of the anisotropy is to apply a higher doping. The underlying mechanisms are twofold: (i) the phase space is reduced and therefore the scattering is weaker and (ii) the doping induced enhancement of the screening decreases the carrier-carrier scattering.

Paper IX is a review article summarizing the insights on the ultrafast phenomena characterizing the carrier dynamics in graphene.

CHAPTER 3

Carrier dynamics in an electric field

In this chapter, the impact of an external in-plane electric field to the carrier dynamics in graphene will be discussed. First, the influence of the field to the carriers, resulting into a dark current is studied. Note that, due to the linear band structure in graphene, carrier-carrier scattering has a crucial role in the generation of the current [57, 76–78]. While most studies in literature focus on the linear response and deploy the Drude approach for the conductivity, there are only a few studies addressing the non-linear response of graphene to an electric field [79–83]. In our microscopic theory, we investigate the interplay of field induced shift of carriers and many-particle scattering.

3.1 Field induced shift of carriers

An external electric field, which is set to point into the negative x-direction, $\mathbf{E} = (-E,0,0)$, shifts the carriers in graphene into the opposite direction (positive x-direction). For undoped graphene the dynamic for electrons and

holes is completely symmetric, such that it is sufficient to consider only the electrons in the conduction band. Note that the shift of electrons and holes in the same direction correspond to a moving into opposite directions in real space.

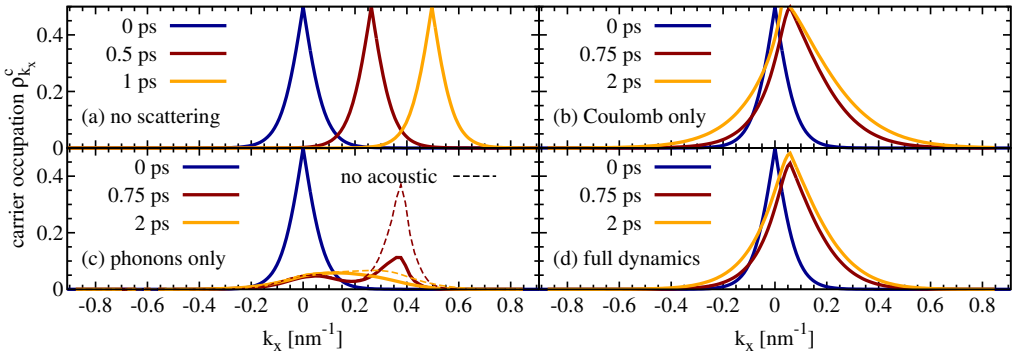

Figure 3.1: *Carrier occupation at different times (with respect to the switch-on of the electric field) for a field strength of* $E = 0.32\,\mathrm{V}\mu\mathrm{m}^{-1}$ *and a temperature of* $T = 300\,\mathrm{K}$ *including (a) no scattering contributions, (b) only carrier-carrier scattering, (c) only carrier-phonon scattering, and (d) full carrier dynamics.*

To understand the impact of the field-induced shift of carriers, the case without scattering will be discussed first. The behaviour of the carrier occupation $\rho^{\mathrm{c}}_{\mathbf{k}}(t)$ (initially a Fermi distribution) along the k_x-direction, which is the same direction of the applied field, is illustrated in Fig. 3.1(a). After switching on the electric field the carriers are shifted into the positive k_x-direction, corresponding to the opposite direction of the field. The shift of the carrier occupation destroys the initial symmetry of the carrier distribution in k space, since now more carriers are on the positive branch of the Dirac cone.

Influence of carrier-carrier scattering

Including now carrier-carrier scattering leads to only a slight shift of carrier distribution, compared to the case without scattering. The redistribution of carriers acts against the electric field (and the corresponding shift of carriers) such that the position of the maximum of the carrier distribution equilibrates, cf. Fig. 3.1(b). Interestingly, the distribution of carriers becomes much broader than the initial Fermi distribution. The underlying mechanism

is a density increase induced by efficient Auger processes, or more specific impact excitation. The field induced shift favors impact excitation in two ways: (i) it provides carriers at high energies and (ii) it depopulates the carrier occupation in the vicinity of the Dirac point, such that one carrier from an energetically higher state scatters to lower energies while a second carrier scatters from the valence band into the conduction band and therefore increases the carrier density. A measure for the density increase is defined by the dark carrier multiplication (dCM) which is the ratio of the final and initial densities n and n_0: $\mathrm{dCM} = \frac{n}{n_0}$. Another possibility to generate more carrier density in the conduction band is the Schwinger mechanism [82–84], but this effect can be neglected at temperatures $T \geq 100\,\mathrm{K}$, such that the field induced dark carrier multiplication outweighs the Schwinger effect.

Influence of carrier-phonon scattering

In the case of pure carrier-phonon scattering the shape of the carrier distribution deviates drastically from a Fermi distribution, cf. Fig. 3.1(c). Even though it looks like the carrier density is strongly reduced, this is not the case and the density changes only slightly. This impression occurs since in Fig. 3.1(c) only the carrier distribution along the k_x axis is depicted, but considering the whole two-dimensional plane in k-space reveals that the carrier distribution is widely broadened, due to the carrier-phonon scattering. In contrast to the carrier dynamics without electric field the scattering with acoustic phonons in the presence of an electric field is crucial, due to the influence of acoustic phonons to momentum relaxation.

The complete dynamics including both carrier-carrier and carrier-phonon scattering is displayed in Fig. 3.1(d). The carrier distribution behaves similar to the case with pure Coulomb processes, where the continuous generation of carriers induce an increasing broadening of the carrier distribution. When the distribution becomes too broad, the efficiency of phonon-induced recombination, which reduces the carrier density, is enhanced. Additionally, the energy relaxation of phonon-intraband scattering then also enhances.

3.2 Dark current

The current density for undoped graphene is given by

$$\mathbf{j}(t) = -\frac{g\, e_0}{\hbar L^2} \sum_{\mathbf{k}} \rho^c_{\mathbf{k}}(t) \nabla_{\mathbf{k}} \varepsilon^c_{\mathbf{k}} = e_0 n(t) \mathbf{v}_{\text{drift}}(t), \tag{3.1}$$

where $g = 8$ accounts for spin and valley degeneracies as well as electron hole symmetry. The second expression can be obtained by introducing the definitions for carrier density $n(t) = (8/L^2) \sum_{\mathbf{k}} \rho^c_{\mathbf{k}}(t)$ (sum of electrons and holes) and using the electron group velocity $\mathbf{v}^c_{\mathbf{k}} = \nabla_{\mathbf{k}} \varepsilon^c_{\mathbf{k}} / \hbar$ to define the drift velocity $\mathbf{v}_{\text{drift}}(t) = -(8/L^2 n(t)) \sum_{\mathbf{k}} \rho^c_{\mathbf{k}}(t) \mathbf{v}^c_{\mathbf{k}}$. The group velocity in conventional materials with parabolic band structure is $\mathbf{v}^c_{\mathbf{k}} = \hbar \mathbf{k}/m$ with effective mass m, this means that the current scales linearly with the shifting of carriers. In contrast, graphene provides a linear band structure with $\varepsilon^c_{\mathbf{k}} = \hbar v_{\text{F}} |\mathbf{k}|$ resulting in $\mathbf{v}^c_{\mathbf{k}} = v_{\text{F}} \mathbf{e}_{\mathbf{k}}$. Note that the group velocity is now independent of the magnitude of the electronic momentum $\mathbf{k}$ and therefore only the angle between $\mathbf{k}$ and the applied electrical field $\mathbf{E}$ counts.

Since the current depends on the carrier density, Auger scattering processes are crucial and have a positive effect on the current density (due to the increase of the carrier density via carrier multiplication).

No scattering

The case without scattering demonstrates that the shift of carriers, which destroys the initial symmetric carrier distribution, leads to an asymmetry even though the shape of the carrier distribtion is not changed. The rise-time of the current is determined by the strenght of the electric field and the current increases until the whole carrier occupation lies completely on the positive side of the Dirac cone. After this, the current rises much slower which is determined by the alignment of the angles to the x-axis, since the current depends on the unity vector $\mathbf{e}_{\mathbf{k}}$. The current saturates when the whole carrier distribution is completely on the x-axis and therefore the angular dependency vanishes.

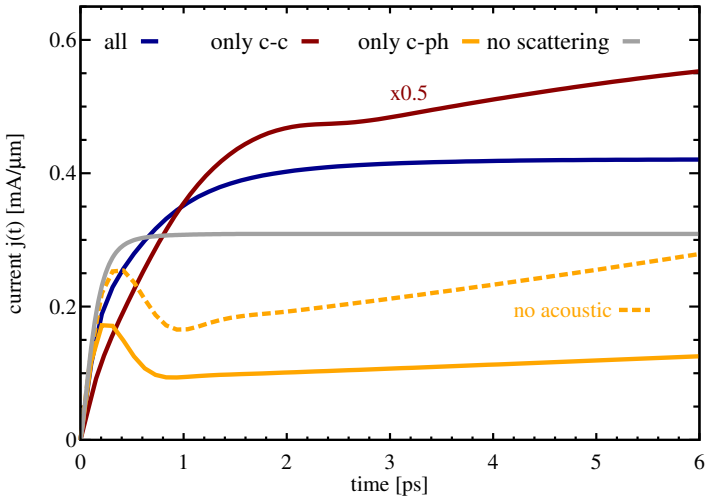

Figure 3.2: *Current for different scattering channels including full carrier dynamics (blue), only carrier-carrier scattering (red, scaled by a factor* 0.5*), only carrier-phonon scattering (orange, dashed without acoustic phonons), and no scattering (grey).*

The equation for the current can then be simplified by using $\sum_{\mathbf{k}} \rho^{\mathrm{c}}_{\mathbf{k}}\, \mathbf{e}_{\mathbf{k}} \approx \mathbf{e}_x \sum_{\mathbf{k}} \rho^{\mathrm{c}}_{\mathbf{k}}$ and the generated saturation current density reads in x-direction

$$j_{\mathrm{sat}} = \frac{8 e_0 v_F}{L^2} \sum_{\mathbf{k}} \rho^{\mathrm{c}}_{\mathbf{k},0} = e_0 v_F n_0 = \frac{e_0 \pi k_B^2}{3\,\hbar^2 v_F} T^2, \tag{3.2}$$

where k_B is the Boltzmann constant and $\rho^{\mathrm{c}}_{\mathbf{k},0}/n_0$ is the initial carrier occupation/density. The saturated current is independent of the strength of the electric field and scales with the square of the temperature T. Note that the saturation of the current density sets in already at picosecond time scales and long before the charge carriers leave the linear region of the Brillouin zone, cf. the grey line in Fig. 3.2. The scenario that carriers leave the linear region of the Brillouin zone, which would eventually result in Bloch oscillations, has not been taken into account, since Coulomb- and phonon-induced scattering processes will prevent this in all realistic situations.

Carrier-carrier scattering

Consider now the case with only carrier-carrier scattering. The efficient Auger processes, which correspond to strong dark carrier multiplication, increase the carrier density. The lack of efficient energy relaxation processes and the field induced shift lead to a permanent generation of carriers. Since the carrier distribution is shifted and the intraband Coulomb scattering redistributes the carriers in such a way that the distribution is more or less symmetric in respect to the maximum, an increase of the density implies that the overall asymmetry increases and therefore also the current, which is shown in Fig. 3.2. In summary, it is not possible to reach a quasi-equilibrium with pure carrier-carrier scattering.

Carrier-phonon scattering

Taking only carrier-phonon scattering with optical phonons into account (dashed orange line in Fig. 3.2), the field induced shift of carriers dominates the first few hundreds femto seconds. The carrier-phonon scattering is suppressed, since the carriers have to be shifted beyond the large phonon energies until carrier-phonon scattering can take place. After the carriers reach these energies, carriers scatter back to lower energies and the field dominates again, this oscillation can be seen in Fig. 3.2. Adding also acoustic phonons (orange line) leads to a much smaller current since the relaxation is now not longer restricted to the discrete phonon energies. Note that carrier-phonon scattering parallel to the Dirac cone can be both intra- or interband process. The field induced shifting of carriers to energetically higher states enables parallel phonon emission processes, the hereby generated phonons are able via absorption to induce parallel interband scattering, resulting into a continously increase of the carrier density which correspond to an ongoing enhancement of the current.

Full dynamics

Considering the complete dynamics including both carrier-carrier and carrier-phonon scattering, the interplay of both scattering mechanisms now exhibits

an equilibrium, since interband emission of optical phonons compete with the density generating Auger processes. This stabilizes the carrier distribution and therefore the current saturates. Note that the current with scattering can be larger than in the case without scattering since (i) the current without scattering saturates and (ii) the efficient dark carrier multiplication increases the carrier density resulting in an enhancement of the current.

CHAPTER 4

Photoconduction effect

In this chapter we study the photoconduction effect in graphene to model photodetectors with high responsivities [85, 86]. This requires the description of the carrier dynamics in presence of an electric field together with optical excitation. In the following, we shine light on the contribution of the carrier multiplication (which generates additional carriers) to the photocurrent and we consider different experimental conditions for tuning the photocurrent.

4.1 Asymmetry and photocurrent

So far, we studied the processes which determine the (asymmetric) carrier distribution before reaching a quasi-equilibrium. In the following section we will discuss how such an asymmetry responds to a pertubation induced by optical excitation, i.e. how the current and the asymmetry changes. The corresponding photocurrent $\mathbf{j}^{ph}(t)$, which is defined as difference between total current $\mathbf{j}(t)$ and stationary current $\mathbf{j}_{\mathrm{sat}}$ before the optical excitation is

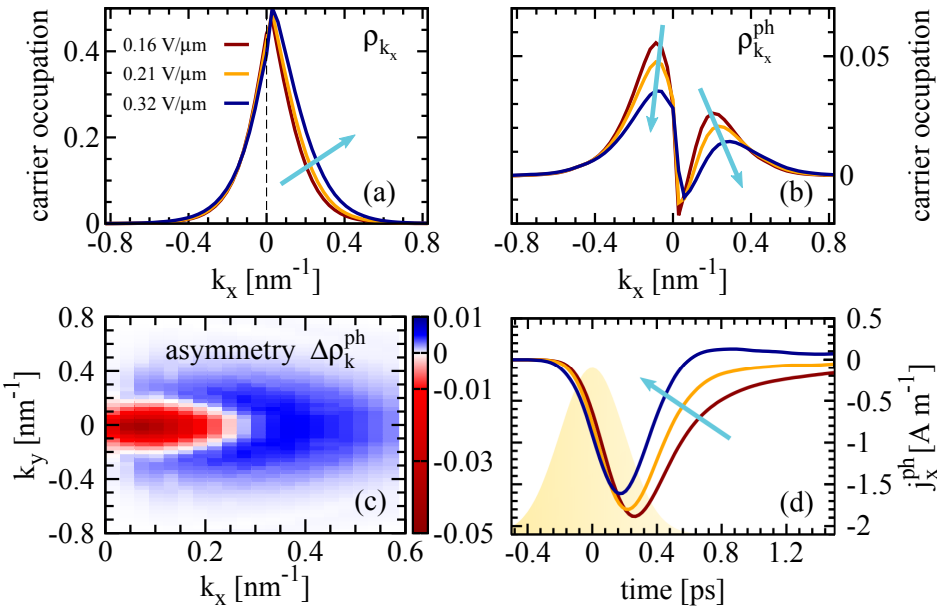

Figure 4.1: *Asymmetry and photocurrent generation. (a) carrier distributions ρ_{k_x} for different electric fields after 0.2 ps of the maximum of the excitation pulse, which is centered at the carrier momentum of 0.5 nm^{-1}. (b) Photo-induced occupation change $\rho^{ph}_{k_x} = \rho_{k_x} - \rho^0_{k_x}$ along the field direction. (c) The asymmetry of the distribution in the k_x-k_y plane which is defined as $\Delta\rho^{ph}_{\mathbf{k}} = \rho^{ph}_{|\mathbf{k}|} - \rho^{ph}_{-|\mathbf{k}|}$ for the chosen field of strength 0.32 Vμm^{-1}. (d) Resulting photocurrent density $j^{ph}_{k_x}$ with the excitation pulse in the background.*

defined as

$$\mathbf{j}^{\mathrm{ph}}(t) = \mathbf{j}(t) - \mathbf{j}_{\mathrm{sat}} = -\frac{g\, e_0 v_{\mathrm{F}}}{L^2} \sum_{\mathbf{k}} \rho^{\mathrm{ph}}_{\mathbf{k}}(t)\, \mathbf{e}_{\mathbf{k}}, \tag{4.1}$$

with the photo-induced occupation change $\rho^{\mathrm{ph}}_{\mathbf{k}}(t) = \rho^c_{\mathbf{k}}(t) - \rho^c_{\mathbf{k},\mathrm{sat}}$. To understand the generation and decay of the photocurrent on a microscopic footing it is necessary to have a closer look to the dynamics of the optically excited carriers $\rho^c_{\mathbf{k}}(t)$.

In Fig. 4.1(a) the carrier occupation ρ_{k_x} is shown for different field strengths, shortly after the maximum of the optical excitation along the x-axis, corresponding to the direction of the applied electric field. The carrier distributions look very similar to the quasi-equilibrium carrier distributions without

optical excitation, which means a Fermi distribution which is shifted and tilted along the direction of the electric field (the effect is more pronounced for stronger fields). To get access to the dynamics induced by the optical excitation, $\rho^{\mathrm{ph}}_{\mathbf{k_x}}$ has to be determined, which is illustrated in Fig. 4.1(b). The maximum of the photo-induced occupation is higher in the negative k_x direction, but the occupation on the positive side of the Dirac cone is much broader. The height of the maximum is determined by two effects: (i) asymmetric optical excitation and (ii) asymmetric scattering. Both mechanisms stem from the shifted quasi-equilibirum distribution which induces different Pauli-blockings on different sides of the Dirac cone, i.e. it is more efficient to excite carriers on the negative side. The same holds for the carrier-carrier and carrier-phonon scattering which is more effective from the positive side to the negative side of the Dirac cone than the other way round. Note that the impact of the asymmetric scattering is in most situations the crucial mechanism. The field induced shift of carriers determines the broadness of the photo-induced occupation resulting into a narrower distribution on the negative side, since the many-particle scattering to lower energies transports the carriers in the same direction as the field, whereas the scattering starting from the positive side of the Dirac cone acts against the shifting and the distribution is broader. The generated photocurrent can be roughly estimated (by neglecting angular dependence) as the asymmetry of the photo-induced carrier distribution $\Delta\rho^{\mathrm{ph}}_{\mathbf{k}} = \rho^{\mathrm{ph}}_{|\mathbf{k}|} - \rho^{\mathrm{ph}}_{-|\mathbf{k}|}$ which is depicted in Fig. 4.1(c) for an electric field with strength $0.32\,\mathrm{V}\mu m^{-1}$. The red and blue areas denote the regions in which the asymmetry is negative and positive. This shows clearly that even though the blue region is more extensive, the red area dominates due to the much larger ampltidue resulting into a negative photocurrent density, which is shown in Fig. 4.1(d).

Applying stronger electrical fields (corresponding to a larger shift of the carriers) strenghten the asymmetry of the carrier distribution since the maximum is shifted farther and the carrier distribution itself becomes more asymmetric by a broader flank in the field direction. Note that a more asymmetric distribution enhances also the asymmetric optical excitation and the asymmetric carrier-carrier and carrier-phonon scattering, but the influence of sufficient high fields on optically generated carriers outperforms these effects resulting into a smaller negative amplitude of the photocurrent. If the field is strong enough, the shift of carriers into the field direction is faster than the asymmetric scattering into the opposite direction, and even positive amplitudes

of the photocurrent can be observed, cf. Fig. 4.1(d).

In summary, the dynamics of optically excited carriers in the presence of an electric field, forming the photocurrent can be traced back to four mechanisms.

i. The **asymmetric optical excitation** which correspond to a negative photocurrent. This contribution becomes only important under certain circumstances, like small excitation energies or strongly distorted quasi-equilibrium distributions, e.g. achieved by high temperatures or substrates with high dielectric constants, such that the Pauli-blocking at the excitation energy on different sides of the Dirac cone differ considerably.

ii. The **asymmetric many-particle scattering** favors scattering from the positive side of the Dirac one to the negative side due to a bigger Pauli-blocking on the positive side induced by the shifted quasi-equilibrium carrier distribution, accounting for a negative contribution to the photocurrent.

iii. The carrier-carrier and carrier-phonon scattering bring optically excited carriers to lower energies into the vicinity of the Dirac point. When these carriers are **shifted by the electric field**, the carriers starting on the negative side of the Dirac cone are transported to the positive side, resulting into a positive contribution to the photocurrent. This effect can be enhanced either by stronger field strengths or by suppressing the many-particle scattering, for example with high-dielectric substrates to suppress carrier-carrier scattering. Another possibility is to use high temperatures, which correspond to strong Pauli-blocking due the broadness of the carrier distribution.

iv. Finally, the **carrier-carrier and carrier-phonon scattering relax** the system on a picosecond timescale back to the quasi-equilibirum distribution in the presence of the electric field. The timescale of the build up of the photocurrent by the negative and positive contributions (i)-(iii) is defined by the duration of the optical excitation.

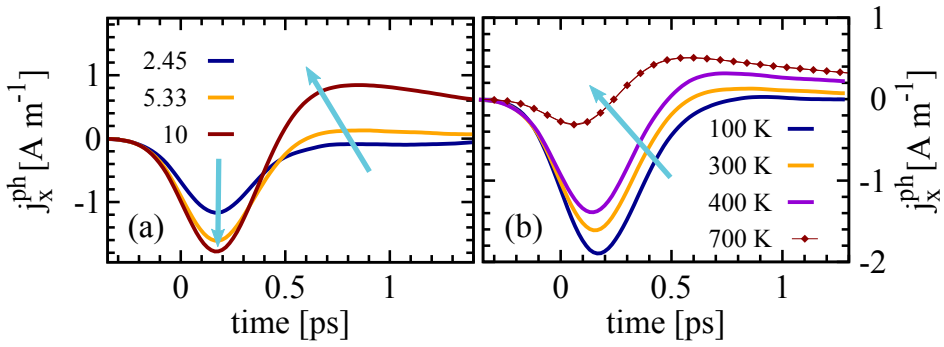

Figure 4.2: *(a) Photocurrent for three different substrates characterized by the dielectric background constants* $\varepsilon_{bg}^{SiO_2} = 2.45$, $\varepsilon_{bg}^{SiC} = 5.33$ *and an exemplary high-dielectric substrate with* $\varepsilon_{bg} = 10$. *(b) Photocurrent for three different temperatures* T, *since the difference of the photocurrent is very small in the range between* $100\,K$ *and* $400\,K$ *we also show the extremely high temperature* $700\,K$.

4.2 Influence of substrate and temperature

Having understood the microscopic mechanisms that govern the photocurrent, we now investigate how it can be controlled by external experimentally accessible quantities, such as temperature and substrate. Our calculations reveal that at enhanced temperatures, the amplitude of the photocurrent density becomes smaller, cf. Fig. 4.2(a). Increasing the temperature corresponds to a much broader distribution with a less pronounced asymmetry in the stationary carrier distribution ρ_k^0 before the optical excitation (Fig. 4.2(b)). Hence, the photocurrent density, which mainly results from asymmetric scattering, becomes smaller. At very large temperatures, we observe the emergence of a positive photocurrent density component approximately 0.2 ps after the optical excitation (blue line in Fig. 4.2(a)). Analogously to the field dependence, the sign of the photocurrent density is determined by the interplay between field-induced shift of the optically excited carriers away from the Dirac point and counteracting many-particle scattering processes bringing the carriers towards the Dirac point.

At high temperatures, the field contribution j_f becomes dominant and gives rise to the observed positive photocurrent. While the initial rise of j_f and the underlying field rate Γ_f remains nearly unchanged with increasing temperatures, the decrease of the scattering rates Γ_s in the first 0.2 ps due to

higher symmetry in the carrier occupation and therefore weaker Pauli blocking is crucial (Fig. 4.2(d)). Since carrier-carrier scattering is more sensitive to Pauli blocking (two electronic scattering processes) the rate decrease with increasing T is more pronounced than in the case of carrier-phonon scattering. In fact, the carrier-phonon rate almost stays constant, since the phonon occupation becomes larger at higher T, compensating the general reduction of the scattering efficiency to a large extent. Note that scattering with K-TO phonons is crucial here, since the strength of the corresponding matrix element is the largest and since its angular dependence favours back scattering across the Dirac cone having the largest impact on the asymmetry of the carrier distribution [39]. Having in mind that scattering induces the negative photocurrent contribution in Fig. 4.2(a) via carrier-phonon and carrier-carrier scattering across the Dirac cone, the reduced many-particle scattering explains the suppression of the negative photocurrent contribution and the eventual emergence of a positive current as the temperature increases.

As we have seen so far, carrier-carrier scattering has a strong impact on the photocurrent density in graphene. It is thus interesting to investigate how it changes for different substrates, since the Coulomb scattering strength can be controlled via the substrate-induced dielectric screening. A higher dielectric constant of the substrate corresponds to a stronger background screening and a weaker carrier-carrier scattering. Figure 4.2(a) shows the temporal evolution of the photocurrent density j_x^{ph} for three different substrates including SiO_2 ($\varepsilon_{bg} = 2.45$), SiC ($\varepsilon_{bg} = 5.33$) and an exemplary high-dielectric substrate ($\varepsilon_{bg} = 10$). The larger ε_{bg}, the stronger is the substrate-induced screening of the Coulomb interaction and the larger is the asymmetry in the carrier occupation ρ_{k_x} (Fig. 4.2(b)) resulting in a more pronounced negative amplitude of the photocurrent density. For substrates with $\varepsilon_{bg} > 5$, we observe the appearance of a positive photocurrent density component approximately 0.5 ps after the optical excitation - similarly to the observation at high temperatures in Fig. 4.2(a). This behaviour is due to the counteracting contributions of the electric field and the many-particle scattering.

While carrier-phonon scattering becomes more efficient for large ε_{bg} due to a higher asymmetry in the carrier occupation, the carrier-carrier scattering is generally strongly reduced through the substrate-induced screening. In particular, the Coulomb-induced asymmetric scattering across the Dirac

cone is strongly suppressed. Additionally, Auger processes are also reduced, leading to a smaller carrier density especially during the duration of the optical excitation, such that the scattering dominates up to 0.5 ps. Moreover, carrier-phonon scattering, which competes with carrier-carrier scattering, is enhanced. In total, the reduction of the field rate and the increased phonon scattering explain the more pronounced negative part of the photocurrent density for high dielectric constants.

4.3 Pulse characteristics

In this section we investigate how the photocurrent can be tuned with respect to the properties of the optical pulse. According to equations (2.1) and (2.2) the pulse is characterized by excitation energy $\hbar\omega_L$, pulse width σ_t, pump fluence E_{pf} and polarisation $\hat{\mathbf{e}}_p$. Fig. 4.3 (a) shows the photocurrent for different pulse parameters, we use as standard pulse parameters $\hbar\omega_L = 600\,\mathrm{meV}$, $\sigma_t = 400\,\mathrm{fs}$, $E_{pf} = 1\,\mu\mathrm{J/cm}^2$ and $\hat{\mathbf{e}}_p = \hat{\mathbf{e}}_y$. Note that the pump fluence is fixed when excitation energy or pulse width are changed. The polarisation dependency for a pulse with large fluence $E_{pf} = 150\,\mu\mathrm{J/cm}^2$ and excitation energy $\hbar\omega_L = 800\,\mathrm{meV}$ is depicted in Fig. 4.3 (b).

Excitation energy

The smaller the excitation energy the stronger is the negative and positive photocurrent. For small excitation energies at $\approx 200\,\mathrm{meV}$ (red curve, Fig. 4.3 (a)) Pauli-blocking is strong and induces enhanced asymmetric excitation resulting into a more pronounced negative photocurrent. Applying optical pulses with small energies induce a more pronounced generation of carriers, since the density of states is low for small energies and therefore the optical excitation is more efficient. The increased density of optically excited carriers correspond to a stronger impact of the field, since more carriers are shifted corresponding to the larger positive photocurrent at later times.

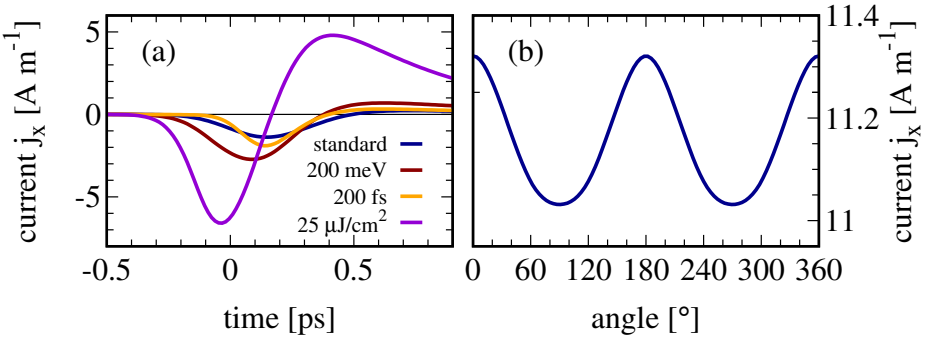

Figure 4.3: *(a) comparison of the photocurrent for different pulse parameters, namely excitation energy, pulse width and pump fluence. (b) amplitude of the photocurrent for strong optical excitation in dependence of the angle of excited carriers, i.e.* 0° *(*90°*) correspond to carriers generated along the x-axis (y-axis).*

Pulse width

With short pulses the negative and positive photocurrent is enhanced (orange curve, Fig. 4.3 (a)). The width of the optical excitation determines how many carriers are excited during one time interval, this means the carrier occupation rises faster for small pulses and therefore a larger carrier occupation is established. For long pulses the carrier occupation is reduced since scattering processes takes place during the optical excitation. The amplitude of the carrier distribution correspond to the out-scattering of carriers such that the asymmetric scattering is enhanced for short pulses and the negative photocurrent is more pronounced. In addition, high occupations provide also good conditions for Auger scattering, especially impact excitation, resulting into a larger number of optically excited carriers which contribute to a stronger positive photocurrent.

Pump fluence

Increasing the pump fluence corresponds to an enhanced excitation of carriers, which leads to a more pronounced negative and positive photocurrent (violet curve, Fig. 4.3 (a)). The negative amplitude of the photocurrent is

enhanced because more carriers are generated which results in better conditions for asymmetric scattering. The positive amplitude of the photocurrent increases too with increasing pump fluence, since the more carriers are generated the more carriers can be shifted by the electric field and contribute to the photocurrent. For stronger pump fluences $\approx 100\,\mu\mathrm{J/cm}^2$ the latter effect of high occupations is dominant and the positive amplitude becomes stronger than the negative amplitude.

Polarisation dependence

Now, we investigate the polarisation dependency of the positive photocurrent. To get well defined positive amplitudes we excite with higher excitation energies ($\hbar\omega_L = 800\,\mathrm{meV}$) to reduce asymmetric excitation and we use a large pump fluence of $E_{pf} = 150\,\mu\mathrm{J/cm}^2$ to have a dominant positive amplitude. In Fig. 4.3 (b) the maximal positive amplitude of the photocurrent is depicted, wheras 0° (90°) means that carriers along the x-axis (y-axis) are generated (corresponding to a pulse polarisation of $\hat{\mathbf{e}}_y$ ($\hat{\mathbf{e}}_x$)). Note that the symmetries of the system provide that angles with a difference of 180° exhibit the same dynamics, the same holds for mirroring along the electric field axis (x-axis), e.g. φ and $-\varphi = 360° - \varphi$.
The amplitude for in (x-direction) excited carriers is the strongest because the asymmetric scattering becomes weaker. Since optically excited carriers in $-x$-direction are shifted towards lower energies which are the same energies in which the asymmetric scattering of carriers is most efficient, i.e. the shift of carriers along the x-axis provide an enhanced Pauli-blocking reducing the asymmetric scattering.

CHAPTER 5

Bolometric effect

In the previous chapters we considered a situation in which the dark current is given by Ohm's law $\mathbf{j} = \sigma\mathbf{E}$ and the corresponding photocurrent is generated by optically excited carriers. This means that the increase of charged carriers changes the conductivity and therefore the photocurrent. In the following section we take into account that a graphene sheet under optical illumination heats up and the enlarged temperature induces a change of the quasi-equilbrium conductivity. This mechanism is called bolometric effect and the corresponding bolometric photocurrent[25] j_{bolo} is given by the change of the quasi-equilibrium conductivity σ with respect to the initial temperature $d\sigma/dT_0 = d^2j/(dT_0dE)$ multiplied by the optically-induced temperature change dT and applied electric field E. Since the current scales linearly with the electric field (due to Ohm's law) it is sufficient to consider dj/dT_0 instead of $Ed\sigma/dT_0$ and the bolomtric photocurrent reads

$$j_{\text{bolo}} = \frac{dj(T_0)}{dT_0} \cdot \Delta T. \tag{5.1}$$

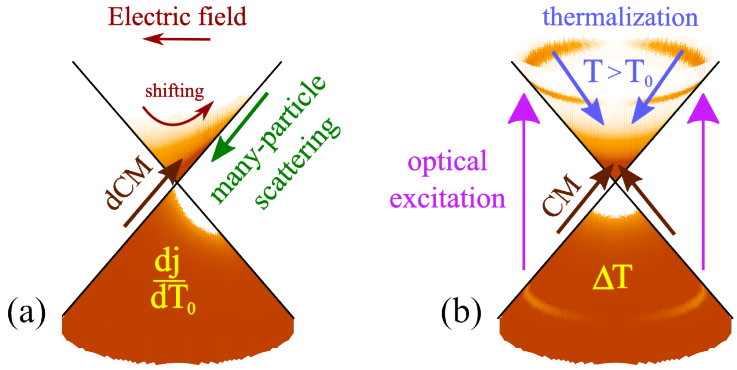

Figure 5.1: *(a) An electric field shifts the carriers in reciprocal space, whereas many-particle scattering counteracts this field-induced shift and brings the hot carriers back to the Dirac point. Due to the linear band structure of graphene, Auger scattering is efficient and results in a dark carrier multiplication (dCM) increasing the charge carrier density. (b) Optical excitation without applied electric field: Photo-excited carriers thermalize to the Dirac point and form a hot Fermi distribution.*

It is difficult to distinguish between the photoconduction and the bolometric effect, since the optical excitation has two effects on the photocurrent, first, the increase of charged carriers and second, the increase of temperature and induced temperature change of the conductivity. To get access to the bolometric effect we investigate the two contributions in equation 5.1 separately (i) the change of the transport current dj/dT_0 with initial temperature T_0 calculated for the case without optical excitation (cf. Fig. 5.1(a)), and (ii) the optically-induced temperature change ΔT which is evaluated for the case without an electric field. (cf. Fig. 5.1(b)).

Since the bolometric effect is known to dominate the photoresponse of biased graphene [33–36], it is crucial to investigate dj_{dark}/dT_0 for a finite doping. An investigation of j_{dark} for different temperatures and doping reveals that it can be significantly increased in doped samples. This is a direct consequence of the increased initial carrier density in the presence of doping.

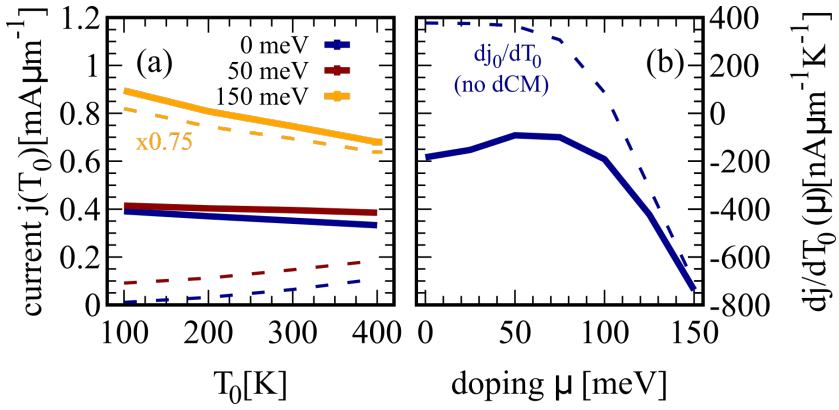

Figure 5.2: *(a) Temperature dependence of current for different doping values. The dashed lines represent the current without dCM. (b) Doping dependence of* dj_0/dT_0 *(without dCM) and* dj/dT_0 *(with dCM).*

5.1 Transport current

The first contribution, i.e. the temperature dependence of the conductivity, is obtained by determining the current density of graphene in a constant electric field at different temperatures. The electric field induces a shift of thermally excited charge carriers away from the Dirac point, while many-particle scattering brings them back and thereby introduces a resistivity. In the absence of optical excitation, the dark current j_{dark} decreases linearly with T_0 for different doping values, cf. Fig. 5.2(a). The temperature dependent decay of the dark current dj_{dark}/dT_0 for different doping values is depicted in Fig. 5.2(b) and shows a minimum of the amplitude at approximately 50 meV (dj_{dark}/dT_0 is negative). Note that our equations of motion are electron-hole symmetric and thus the same current density is found when the sign of the doping is reversed. The doping regime below 50 meV is governed by carrier-carrier scattering and for larger doping values carrier-phonon scattering is the prevailing mechanism.

First, we investigate the behaviour of dj_{dark}/dT_0 for small doping values which is determined by the interplay of the number of charge carriers and many-particle scattering which redistributes the charge carriers and thereby counteracts their shift in the electric field. In graphene, the two factors are not independent of each other, since efficient Auger scattering has an impact on

the carrier density. Auger scattering results in a carrier density increase when graphene is exposed to an external in-plane electric field and the dark carrier multiplication is the dominant mechanism behind the observed behaviour of the dark current for doping values below 50 meV. In undoped graphene the strong dCM and the corresponding increase of charged carriers for low temperatures results into an enhanced dark current and the temperature dependence of the current is steep. The dashed lines in Fig. 5.2 show that increasing the doping level leads to weaker dCM, since more states are occupied at low energies and the collinear Auger-type scattering does not longer occur near the Dirac point, where it bridges the valence and the conduction band, but it becomes a regular intraband scattering channel at higher energies. As a result the temperature dependence of the dark current becomes flatter, i.e. the absolute value of dj_{dark}/dT_0 decreases.

At higher doping values, i.e. doping values larger than 50 meV, the impact of carrier-phonon scattering rises drastically and consequently dj/dT_0 eventually decreases. The reason for the enhanced carrier-phonon scattering is that the carrier distribution for higher doping values is much broader and enables relaxation via optical phonons such that the current becomes more sensitive to temperature changes and therefore also the conductivity shows a sizeable variation with temperature.

5.2 Temperature increase

Now, we consider the situation without electric field but with optical excitation. The graphene layer is excited with a laser pulse with energy $\hbar\omega_L = 0.6\,\mathrm{eV}$ and with a pump fluence of $1\,\mu\mathrm{Jcm}^{-2}$. The excited carriers relax towards lower energies and redistribute the carrier distribution via many-particle scattering in such a way that the carriers form a hot Fermi distribution, for more informations see chapter 2.

The dependence of the temperature change ΔT on initial temperature and doping is depicted in Fig. 5.3 and exhibit a maximum around 70 meV. The increase of temperature for doping values below 70 meV is a result of the increasing phase space for holes in the valence band between optical excitation and Fermi level which leads to a smooth transition from the excitation energy

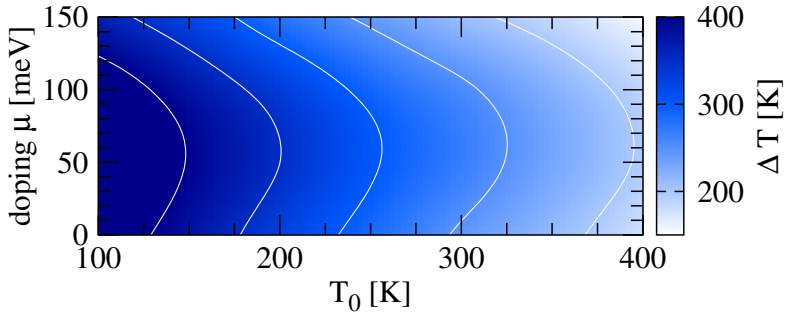

Figure 5.3: *Maximal temperature increase ΔT (with respect to the initial temperature T_0) after optical excitation as a function of doping μ and T_0 at a fixed pump fluence of $1\mu J/cm^2$.*

to the Fermi level resulting in a broader carrier distribution and therefore a higher temperature. For larger doping the phase space induced temperature increase saturates, since the phase space for electrons in the conduction band gets smaller and at sufficient high doping values the Fermi level is so close to the excitation energy that carrier scattering becomes weaker due to Pauli-blocking and the increase of temperature decreases. The following decrease of temperature for doping values above 70 meV is governed by the significant increase of the charge carrier density since the Fermi level shifts to energies with higher density of states. As a result, the energy induced by optical excitation, can be distributed to more carriers and therefore the energy per carrier decreases, which corresponds to a reduced temperature.

In conclusion, for small doping values the phase space increase in the valence band determines the increase of temperature and for large doping the redistribution of energy to more carriers results into a decrease of temperature.

5.3 Bolometric photocurrent

Finally, we combine the two contributions dj/dT_0 and ΔT to determine the bolometric photocurrent j_{bolo}, according to equation 5.1. The bolometric photocurent as function of doping for different temperatures is depicted in

Fig. 5.4 and shows essentially the same behaviour as dj/dT_0 with an additional temperature dependent parabolic distortion due to $\Delta T(T_0)$, cf. Fig. 5.3. The bolometric photocurrent is negative with a minimal amplitude at a doping of 50 meV. The current is slightly larger at lower doping values and becomes significantly increased for doping values larger then 100 meV. This reflects exactly the behaviour of dj/dT_0 shown in Fig. 5.2(b). The bolometric photocurrent is enhanced at lower temperatures (Fig. 5.4), which stems from a larger photo-induced temperature change ΔT, as shown in Fig. 5.3.

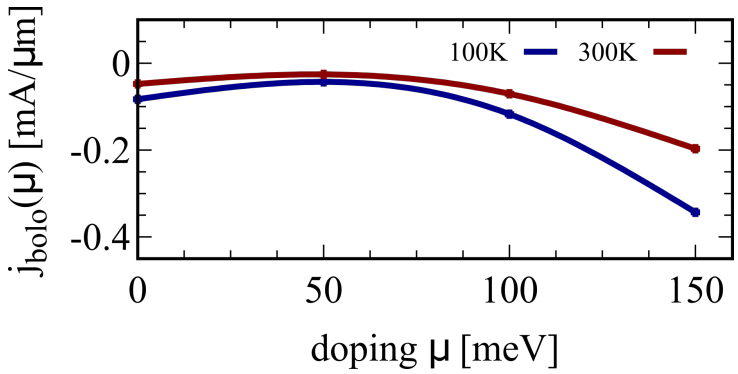

Figure 5.4: *Bolometric photocurrent for two different temperatures in dependence of doping. The amplitude of the photocurrent exhibit a minimum at 50 meV reflecting the behaviour of* dj/dT_0.

CHAPTER 6

Spatio-temporal carrier dynamics

Until now, we studied the carrier dynamics in spatial homogeneous situations, but for optoelectronic applications, where carrier transport phenomena play an important role it is crucial to understand the spatio-temporal carrier dynamics. So far, there have been only a few studies on spatio-temporal dynamics and diffusion in graphene [87–89] and other low dimensional materials, such as carbon nanotubes[90] and transition metal dichalcogenides[91–94].

In this chapter we study spatial inhomogeneous systems and determine the spatio-temporal carrier dynamics. We consider a graphene sheet under local optical excitation, see Fig. 6.1 (red arrows). After the excitation in region II, carriers relax to lower energies via Coulomb scattering (orange arrows) and phonon-induced scattering (green arrows). Since the excitation is local there are spatial gradients of the carrier density, which causes diffusion of exited carriers towards spatial positions with lower densities (purple arrows), i.e. region I and III. In this work we will investigate the dynamics of carriers along the x-axis going through the regions I-III. We excite carriers with a 200 fs optical pulse with energy 1 eV and fluence $1\mu\mathrm{J/cm}^2$ which has a spatial Gaussian profile.

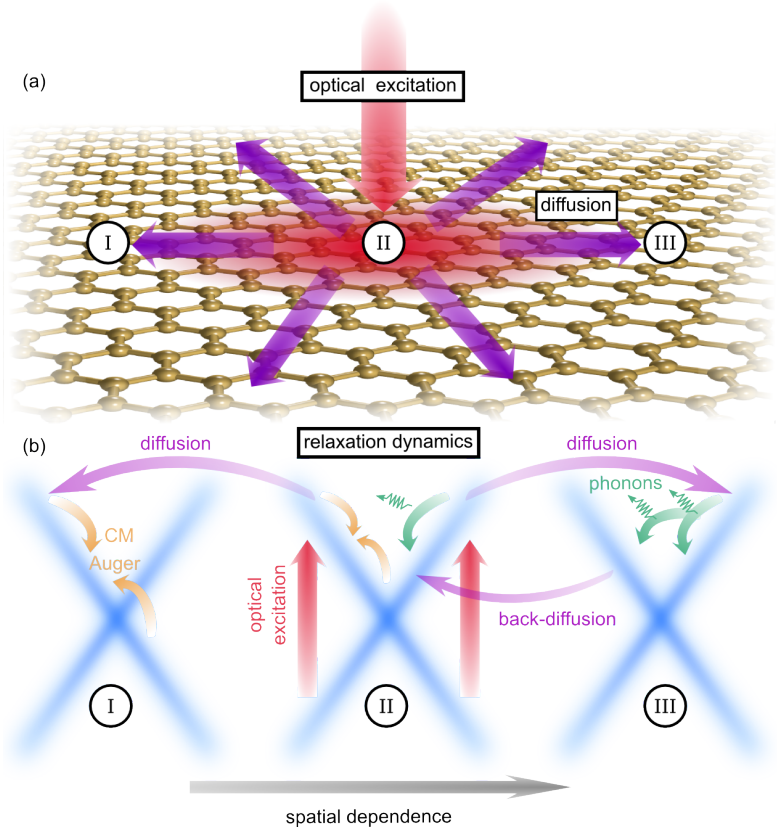

Figure 6.1: *(a) Optically excited carriers in spatial region II diffuse to regions I and III. (b) Many-particle scattering leads to relaxation. Back-scattering via carrier-phonon scattering and resulting back-diffusion counteract the diffusion.*

The term $\nabla_{\mathbf{k}} \varepsilon^{\lambda}_{\mathbf{k}}/\hbar \cdot \nabla_{\mathbf{r}} f^{\lambda}_{\mathbf{k}}(\mathbf{r},t)$, cf. equation (1.72), leads to diffusion of carriers, in such a way that carriers diffuse into the same spatial direction as their momentum points $\nabla_{\mathbf{k}} \varepsilon^{\lambda}_{\mathbf{k}} \propto \mathbf{e}_{\mathbf{k}} = \mathbf{k}/|\mathbf{k}|$. For example electrons with positive/negative momentum move into positive/negative direction in space, see Fig. 6.1 (b). Note that holes move into the opposite direction. In Fig. 6.3 (a) we evaluate the spatio-temporal carrier dynamics without scattering. Carriers are excited around the origin in position with a radius of $\approx 200\,\mathrm{nm}$. After approximately 100 fs, carriers with different signs in momentum are separated by diffusion and the initial spatial peak splits up into two peaks of the same width but with half of the density. Therefore carriers with different signs in momentum separate, which generate locally asymmetric carrier

distributions in momentum space resulting into local currents $\mathbf{j}(\mathbf{r},t)$, cf. Fig. 6.3 (b). Note that in a homogeneous system the mean current vanishes.

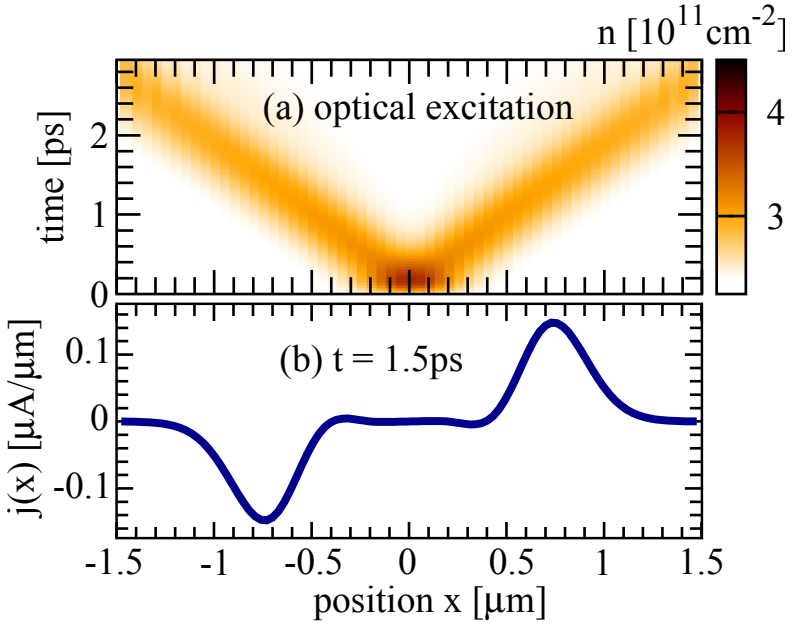

Figure 6.2: *No scattering: (a) After optical excitation the carrier densities with different sign of momenta splits up. (b) Spatial dependence of the current after* 1.5 *ps.*

6.1 Diffusion and scattering

Now, we investigate the behaviour of different scattering mechanisms under the influence of diffusion. The spatio-temporal evolution of the optically excited carrier density is depicted in Fig. 6.3 (a), where we included carrier-phonon scattering. The density at the spatial origin decreases with time which is a result of phonon-induced relaxation processes. The broadening of the density in position remains almost the same, which means that the carrier-phonon scattering counteracts the diffusion via back-scattering and following back-diffusion (see Fig. 6.1), which will be discussed later in more detail.

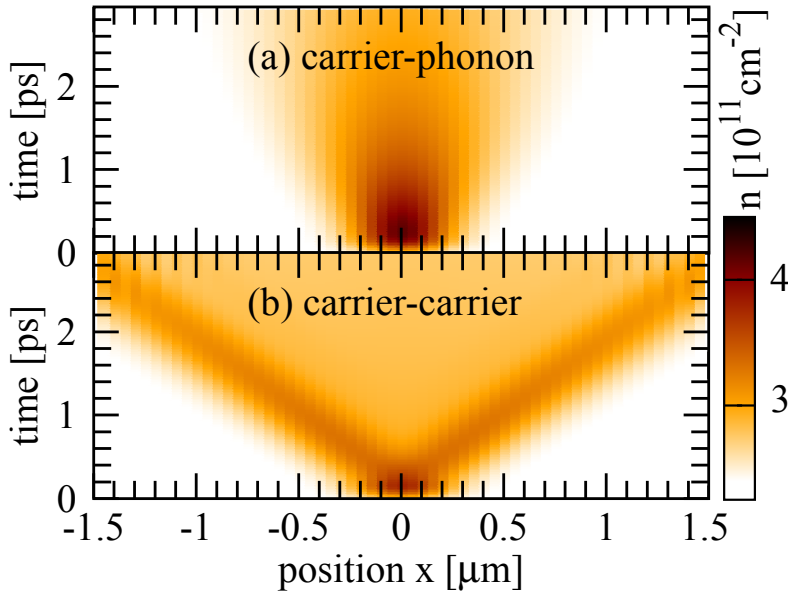

Figure 6.3: *(a) Optical excitation and carrier-phonon scattering: The carrier distribution becomes smaller with time, due to back-scattering via phonons and following back-diffusion. (b) Optical excitation and carrier-carrier scattering: The carrier density increases with time due to CM and gets broader.*

Finally, we consider the case with optical excitation together with carrier-carrier scattering (see Fig. 6.3 (b)). The carrier density diffuses with the same speed as in the case without scattering (cf. Fig. 6.2 (a)). This is a consequence of the symmetries of the carrier-carrier scattering which favors parallel scattering and momentum flipping processes are very inefficient. In contrast to the case without scattering the spatial region between the both peaks contains carriers. This is a result of inefficient scattering processes which scatter carriers from one side of the Dirac cone to the other side.

Carrier-phonon dynamics

To get a deeper understanding of the underlying processes of the spatio-temporal carrier dynamics we investigate the spectral and spatial behaviour of the Wigner function for different times. In 6.4 (a) and (b) we substracted

show the change of the Wigner compared to the initial situation $t = -\infty$, i.e. $\tilde{f}_k(x,t) = f_k(x,t) - f_k(x,-\infty)$. We start with the interplay between diffusion and carrier-phonon scattering after optical excitation. The optically excited carriers scatter via optical phonons to lower energies and form new peaks in the spectral distance of the phonon energy (red lines in Fig. 6.4 (a), note that in this figure the initial Fermi distribution is subtracted). Diffusion processes lead to a spatial broadening of the carrier distribution and after 1 ps the carriers relaxed to low energies (cf. Fig. 6.4 (b)). To investigate the impact of diffusion in more detail we performed the same calculation twice but in the second computation we excluded diffusion. By looking at the difference of both calculations we can directly see the influence of diffusion to carrier-phonon scattering. As already mentioned in the theory section carriers with positive/negative momentum diffuse to positive/negative positions. This behaviour is depicted in Fig. 6.4 (c), where carriers with positive momentum are removed from negative positions (orange spots) and added to positive positions (red spots). After 1 ps the carriers relaxed to energies below the optical phonon energy and the scattering with acoustic phonons becomes dominant. Since acoustic phonons play a crucial role for the angular relaxation, carriers with positive momenta are scattered to negative momenta and vice versa. The inversion of momenta results into back-diffusion (cf. Fig. 6.1 (b) III), such that the overall carrier distribution becomes narrower in space, cf. Fig. 6.3 (b). The back-diffusion is shown in Fig. 6.4 (d) by the inversed colored regions (red to orange and vice versa) close to the Dirac point.

Carrier-carrier dynamics

Next we investigate the impact of diffusion to carrier-carrier scattering after optical excitation. Intraband carrier-carrier scattering is determined by the Coulomb matrix element and the directional dependence (in momentum space) of the scattering is given by the form factor $\propto 1 + e^{i\varphi}$, with scattering angle φ. This means that parallel scattering ($\varphi = 0$) is the preferable scattering channel, and for back-scattering ($\varphi = \pi$) the amplitude of the Coulomb matrix element vanishes, and therefore it is not possible to back-scatter with carrier-carrier processes. As a result, scattering processes which change the sign of the carrier momentum are inefficient and carriers with positive and

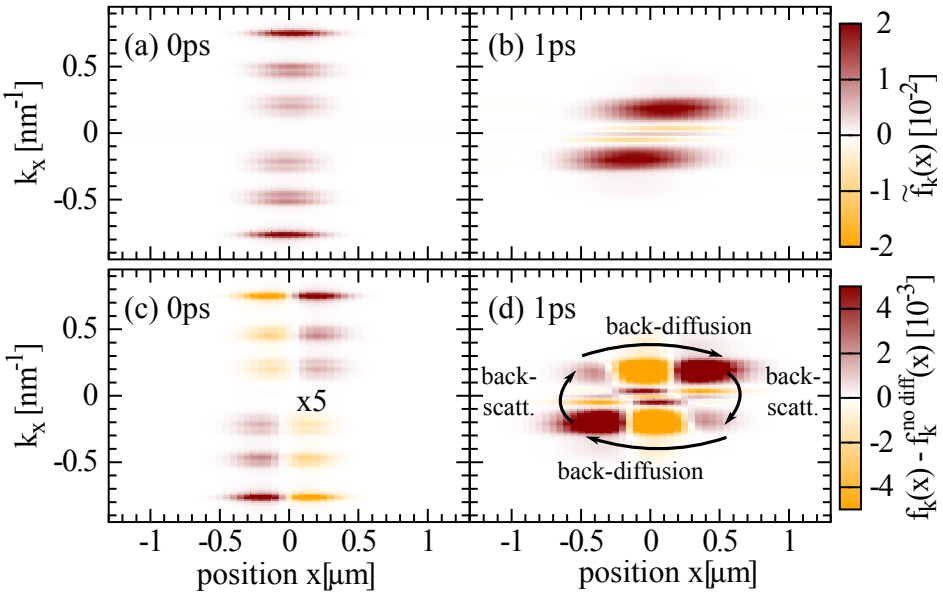

Figure 6.4: *Optical excitation and carrier-phonon scattering. (a), (b): Wigner function for space and momentum for a given time (difference to the initial time). (c), (d): Wigner function (case without diffusion subtracted). Carriers scatter mainly via optical phonons to lower energies, while the overall spatial carrier distribution becomes broader for larger momenta due to diffusion. At* 1 *ps back-scattering with acoustic phonons dominates the dynamics and form additional peaks at low energies. Since the momentum of the carriers is flipped they diffuse back and the spatial distribution becomes smaller.*

negative momenta are separated with respect to the position, similar to the case without scattering (cf. Fig. 6.3).

6.2 Diffusion coefficient

Finally, we investigate the interplay of diffusion together with all relaxation processes after optical excitation, i.e. carrier-phonon as well as carrier-carrier scattering is considered. The relaxation and diffusion of optically induced density is shown in Fig. 6.5 (a). Due to carrier multiplication the carrier density increases after optical excitation. The diffusion is reduced due to carrier-phonon scattering and resulting back-diffusion. To highlight the dif-

fusion we normalized the density in Fig. 6.5 (b). To quantify the diffusion we fit a Gaussian to the diffused carrier density via $\exp(-x^2/w^2)$ for every time step. The temporal evolution of the width w of the Gaussian is depicted in Fig. 6.5 (c), which is connected to an effective diffusion coefficient D via[95] $w^2 = w_0^2 + 4D\,t$. The determined diffusion coefficient is around $360\mathrm{cm}^2/s$ and fits well to experimental data[96, 97]. The diffusion coefficient can be translated into an effective mobility μ by using the Einstein relation[98] $\mu = e_0 D/(k_B T)$. At room temperature we obtain a carrier mobility of approximately $14000\,\mathrm{cm}^2/\mathrm{Vs}$ which is in the range of experimentally reported values[99, 100].

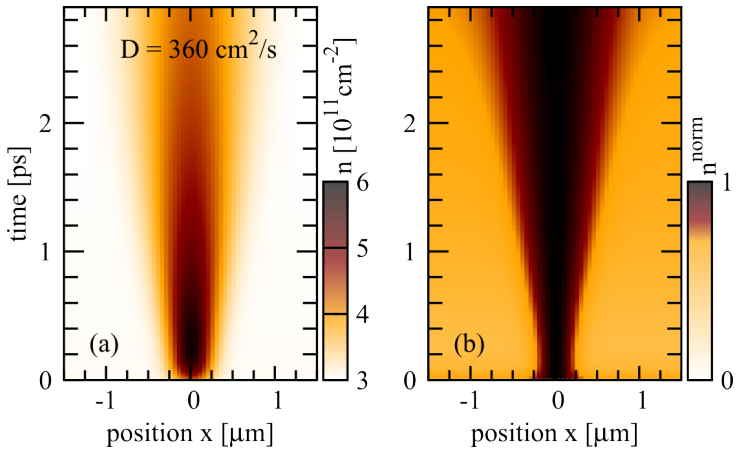

Figure 6.5: *(a) Dynamics of the carrier density after optical excitation including all scattering mechanisms the temporal evolution of the width of the distribution correspond to a diffusion coefficient of $D = 360\,cm^2/s$. (b) Carrier density normalized to the maximal density at each time step to highlight the diffusion of carriers.*

Tuning the diffusion

The diffusion coefficient can be tuned by the experimentally accessible parameters pump fluence, substrate and temperature, cf. Fig. 6.6 (a). The diffusion becomes less efficient with increasing pump fluence (blue curve) due to hot-phonon enhanced back-scattering, this process is depicted in Fig. 6.6 (b). For large fluences more carriers are excited in the middle regions II and III resulting in an increased number of emitted phonons. After a

diffusion process, there are only carriers with negative momenta in region II. The back-scattering occurs now in two different ways: (i) back-scattering from higher energies to lower energies by emitting a phonon and (ii) back-scattering by absorbing a hot phonon. The enhanced back-scattering gives rise to additional channels for back-diffusion resulting in a smaller diffusion coefficient for large pump fluences.

The diffusion coefficient is almost independent of the substrate (red curve),

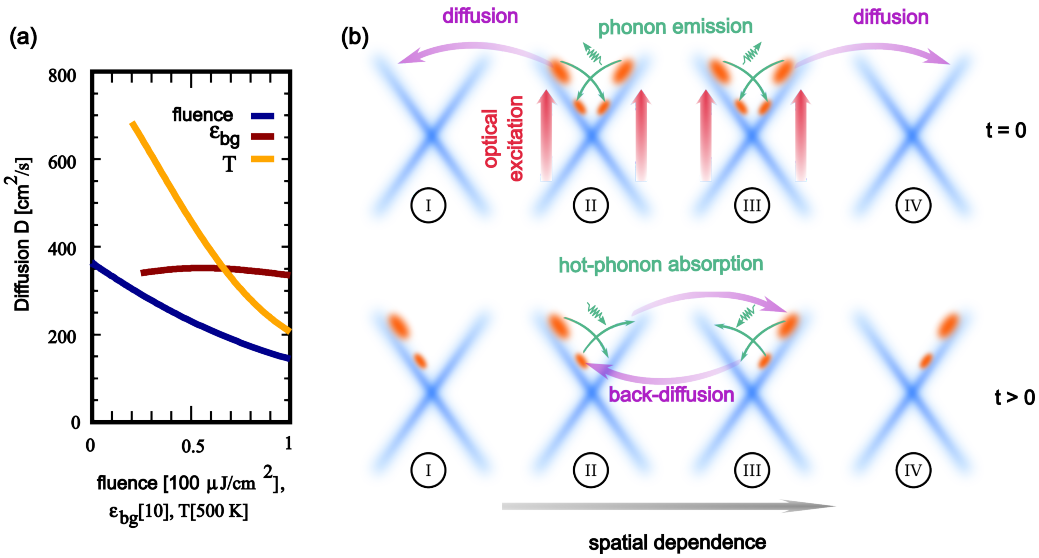

Figure 6.6: *(a) Diffusion coefficient as a function of different pump fluences, substrates and temperatures. The x-axis is normalized to the maximal value of the respective parameter. (b) Illustration of hot-phonon enhanced back-diffusion, which is important for large pump fluences.*

since the substrate determines the strength of the Coulomb interaction (via screening), which play only a minor role for the diffusion of carriers. Finally, we observe that the diffusion can be most efficiently tuned by varying the temperature (orange curve). The lower the temperature, the weaker the carrier-phonon scattering, the less efficient the back-scattering and back-diffusion resulting in a considerably increased diffusion coefficient.

6.3 Thermoelectric effect

The photocurrent induced by the thermoelectric effect stems from spatial gradients of temperature, which are generated due to optical excitation. In a first study we consider a undoped graphene sheet, i.e. we neglect contributions from the photovoltaic effect which correspond to gradients of doping. To create a non-vanishing total current we introduce a spatial inhomogeneity. We assume that the graphene sheet lies on two different substrates in the xy-plane, such that it is on SiC for the half-plane in $-x$-direction, and on SiO_2 for the half-plane in $+x$-direction. This means that the system is homogeneous in y-direction and there is an interface at $x = 0$ between the two different substrate regions.

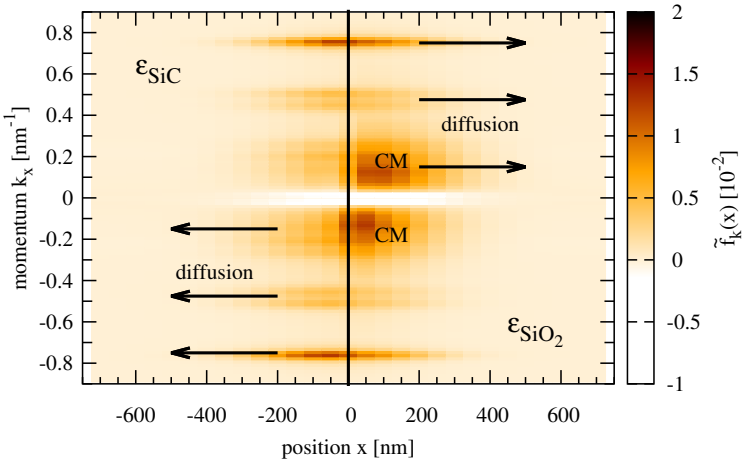

Figure 6.7: *Wigner function (difference to the intial time) for position and momentum* 50 *fs after the optical excitation. The larger screening on the SiC side reduces the carrier multiplication leading to a asymmetric carrier distribution.*

After optical excitation at the interface the carriers relax towards lower energies and the carrier multiplication increases the carrier occupation at low energies. Since the substrate determines the screening and therefore the strength of Coulomb processes like impact excitation, the carrier multiplication is stronger on the SiO_2 side ($\varepsilon_{bg}^{SiC} < \varepsilon_{bg}^{SiO_2}$), cf. Fig. 6.7. This results into a spatial asymmetric distribution of excited carriers and their corresponding

carrier temperature. Since diffusion take place already during the process of carrier multiplication, carriers with negative momenta from the SiO_2 side diffuse into the SiC side and induce a Pauli-blocking reducing the carrier multiplication which leads to a positive photocurrent shortly after the excitation, cf. 6.8 (b). Due to the temperature difference at the interface the gradient towards the SiC side is larger and the carrier diffusion into the $-x$-direction is pronounced (Fig. 6.8 (a)) such that the corresponding current is larger than the current in the $+x$-direction and the total current becomes negative (Fig. 6.8 (b)). Additionally, the carrier relaxation via carrier-carrier scattering is enhanced on the SiO_2 side such that less carriers contribute to the positive part of the total current.

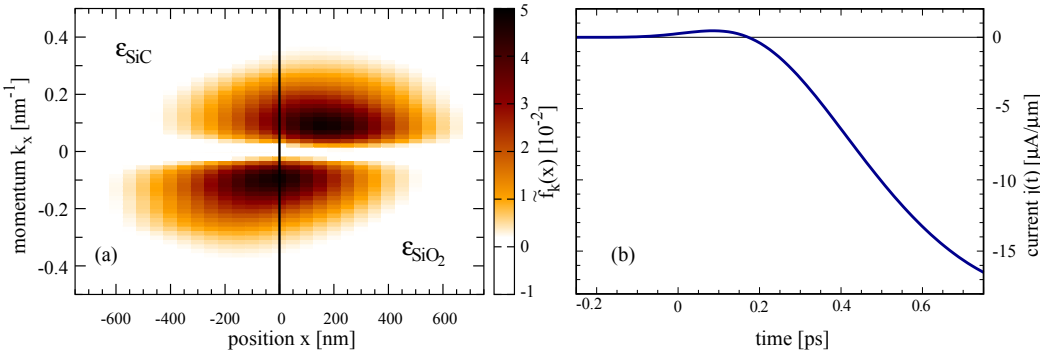

Figure 6.8: *(a) Wigner function (difference to the intial time) for position and momentum* 750 *fs after the optical excitation. The distributions for different sign in momenta are asymmetric due to larger diffusion and slower relaxation in the SiC side. (b) Photocurrent which is generated by a spatial inhomogeneity induced by different substrates.*

In further studies we want to consider the spatio-temporal dynamics in the presence of an electric field, which is created by diffusing carriers and given by the Poisson equation, to model a p-n junction and determine the photovoltaic and thermoelectric effect.

CHAPTER 7

Summary and outlook

In this thesis the spatio-temporal dynamics of optically excited carriers in graphene has been discussed. In the beginning, we investigated the relaxation dynamics (paper IX), proposed a graphene based laser (paper VI) and we determined how the relaxation channels can be tuned (paper V). Additionally, we described saturation effects (paper VII, VIII), Auger scattering (paper XI) which induces efficient carrier multiplication, anisotropy of excited carriers (paper X).

Afterwards we focused on transport mechanisms in graphene to describe photodetection. In graphene the photodetection relies on different mechanisms such as photoconduction, bolometric, photovoltaic and thermoelectric effect. The photoconduction and the bolometric effect appear in biased graphene whereas the photovoltaic and thermoelectric effect are determined by spatial gradients of doping and temperature.

By studying the carrier dynamics in the presence of an electric field without optical excitation we showed that under certain circumstances the current

becomes larger than the current without scattering, which can be traced back to the efficient density increase due to dark carrier multiplication (paper IV). Considering also optical excitation, we investigated how asymmetric scattering and asymmetric excitation generate a negative photocurrent (paper III) and we studied different experimental scenarios (excitation energy, pump fluence, pulse width, polarisation direction, different substrates, temperature and fields). We presented the bolometric effect and showed that this effect is strongest for large doping values (paper II) which is a result of the change of conductivity (or current) with temperature as function of doping.

We investigated the spatio-temporal carrier dynamics by using the Wigner representation and we determined the interplay of diffusion processes and many-particle scattering (paper I). We showed that back-scattering via carrier-phonon scattering and back diffusion are crucial to prevent the spatial separation of carriers with different momenta. Understanding spatial effects on the carrier dynamics enabled us to get first insights into the thermoelectric effect.

Acknowledgments

It is a pleasure to thank all the people who helped me to write the thesis. First of all, I would like to thank my supervisor Ermin Malic for his excellent guidance and support. I also thank my examiner Jari Kinaret for constructive comments and advices. I thank Andreas Isacsson for being my second supervisor. I am grateful to Doris Reiter and the committee members for reviewing my thesis. Furthermore, I would like to thank the whole work group at Chalmers for fruitfull discussions. I also thank my collaborators at TU Berlin. Special thanks to my parents, family and friends for encouraging me and being there.

Bibliography

[1] R. E. Peierls, Nano Lett. **5**, 177 (1935).

[2] K. S. Novoselov, A. K. Geim, S. V. Morozov, D. Jiang, Y. Zhang, S. V. Dubonos, I. V. Grigorieva, and A. A. Firsov, Science **306**, 666 (2004).

[3] A. K. Geim and K. S. Novoselov, Nature Mater. **6**, 183 (2007).

[4] A. C. Ferrari et. al, Nanoscale **7**, 4598 (2015).

[5] T. Winzer, A. Knorr, and E. Malic, Nano Lett. **10**, 4839 (2010).

[6] D. Brida, A. Tomadin, C. Manzoni, Y. J. Kim, A. Lombardo, S. Milana, R. R. Nair, K. S. Novoselov, A. C. Ferrari, G. Cerullo, and M. Polini, Nature Commun. **4**, 1987 (2013).

[7] F. Wendler, A. Knorr, and E. Malic, Nature Commun. **5**, 3703 (2014).

[8] T. Winzer and E. Malic, Phys. Rev. B **85**, 241404 (2012).

[9] F. Kadi, T. Winzer, A. Knorr, and E. Malic, Sci. Rep. **5**, 16841 (2015).

[10] T. Plötzing, T. Winzer, E. Malic, D. Neumaier, A. Knorr, and H. Kurz, Nano Lett. **14**, 5371 (2014).

[11] M. Mittendorff, F. Wendler, E. Malic, A. Knorr, M. Orlita, M. Potemski, C. Berger, W. A. de Heer, H. Schneider, M. Helm, and S. Winnerl, Nature Phys. **11**, 75 (2015).

[12] I. Gierz, M. Mitrano, J. C. Petersen, C. Cacho, I. C. E. Turcu, E. Springate, A. Stöhr, A. Köhler, U. Starke, and A. Cavalleri, journal of Physics: Condensed Matter **27**, 164204 (2015).

[13] S. V. Morozov, K. S. Novoselov, M. I. Katsnelson, F. Schedin, D. C. Elias, J. A. Jaszczak, and A. K. Geim, Phys. Rev. Lett. **100**, 016602 (2008).

[14] A. H. Castro Neto, F. Guinea, N. M. R. Peres, K. S. Novoselov, and A. K. Geim, Rev. Mod. Phys. **81**, 109 (2009).

[15] S. Das Sarma, H. E. H. Adam, S., and E. Rossi, Rev. Mod. Phys. **83**, 407 (2011).

[16] F. Xia, T. Mueller, Y.-M. Lin, A. Valdes-Garcia, and P. Avouris, Nature Nano. **4**, 839 (2009).

[17] T. Mueller, F. Xia, and P. Avouris, Nat. Photon. **4**, 297 (2010).

[18] T. Echtermeyer, L. Britnell, P. Jasnos, A. Lombardo, R. Gorbachev, A. Grigorenko, A. Geim, and K. Novoselov, Nature Commun. **82**, 458 (2011).

[19] M. Furchi, A. Urich, A. Pospischil, G. Lilley, K. Unterrainer, H. Detz, P. Klang, A. M. Andrews, W. Schrenk, G. Strasser and T. Mueller, Nano Lett. **12**, 2773 (2012).

[20] Z. Sun and H. Chang, ACS Nano **8**, 4133 (2014).

[21] Z. Sun, T. Hasan, F. Torrisi, D. Popa, G. Privitera, F. Wang, F.Bonaccorso, D. M. Basko and A. C. Ferrari, ACS Nano **4**, 803 (2010).

[22] T. H. F. Bonaccorso, Z. Sun and A. C. Ferrari, Nature Photon. **4**, 611 (2010).

[23] P. Avouris and C. Dimitrakopoulos, Mater. Today **15**, 86 (2012).

[24] F. H. L. Koppens, T. Mueller, P. Avouris, A. C. Ferrari, M. S. Vitiello, and M. Polini, Nat. Nano. **9**, 780 (2014).

[25] M. Buscema, J. O. Island, D. J. Groenendijk, S. I. Blanter, G. A. Steele, H. S. J. van der Zant, and A. Castellanos-Gomez, Chem. Soc. Rev. **44**, 3691 (2015).

[26] E. J. H. Lee, K. Balasubramanian, R. T. Weitz, M. Burghard, and K. Kern, Nat. Nano. **3**, 486 (2008).

[27] J. Park, Y. H. Ahn, and C. Ruiz-Vargas, Nano Lett. **9**, 1742 (2009).

[28] F. Xia, T. Mueller, R. Golizadeh-Mojarad, M. Freitag, Y.-M. Lin, J. Tsang, V. Perebeinos, and P. Avouris, Nano Lett. **9**, 1039 (2009).

[29] X. Xu, N. M. Gabor, J. S. Alden, A. M. van der Zande, and P. L. McEuen, Nano Lett. **10**, 562 (2010).

[30] N. M. Gabor, J. C. W. Song, Q. Ma, N. L. Nair, T. Taychatanapat, K. Watanabe, T. Taniguchi, L. S. Levitov, and P. Jarillo-Herrero, Science **535**, 648 (2011).

[31] M. Freitag, T. Low, and P. Avouris, Nano Lett. **13**, 1644 (2013).

[32] T. J. Echtermeyer, P. S. Nene, M. Trushin, R. V. Gorbachev, A. L. Eiden, S. Milana, Z. Sun, J. Schliemann, E. Lidorikis, K. S. Novoselov, and A. C. Ferrari, Nano Lett. **14**, 3733 (2014).

[33] M. Freitag, T. Low, F. Xia, and P. Avouris, Nature Photon. **7**, 53 (2013).

[34] M. Mittendorff, S. Winnerl, J. Kamann, J. Eroms, D. Weiss, H. Schneider, and M. Helm, Applied Physics Letters **103**, 021113 (2013).

[35] M. Mittendorff, J. Kamann, J. Eroms, D. Weiss, C. Drexler, S. D. Ganichev, J. Kerbusch, A. Erbe, R. J. Suess, T. E. Murphy, S. Chatterjee, K. Kolata, J. Ohser, J. C. König-Otto, H. Schneider, M. Helm, and S. Winnerl, Opt. Express **23**, 28728 (2015).

[36] S. Schuler, D. Schall, D. Neumaier, L. Dobusch, O. Bethge, B. Schwarz, M. Krall, and T. Mueller, Nano Lett. **16**, 7107 (2016).

[37] E. Malic and A. Knorr, *Graphene and Carbon Nanotubes: Ultrafast Optics and Relaxation Dynamics* (Wiley-VCH, 2013).

[38] H. Haug and S. W. Koch, *Quantum Theory of the Optical and Electronic Properties of Semiconductors* (World Scientific, 2009).

[39] E. Malic, T. Winzer, E. Bobkin, and A. Knorr, Phys. Rev. B **84**, 205406 (2011).

[40] A. Grüneis, R. Saito, G. G. Samsonidze, T. Kimura, M. A. Pimenta, A. Jorio, A. G. SouzaFilho, G. Dresselhaus and M. S. Dresselhaus, Phys. Rev. B **67**, 165402 (2003).

[41] S. Reich, J. Maultzsch, C. Thomsen and P. Ordejn, Phys. Rev. B **66**, 035412 (2002).

[42] G. Czycholl, *Theoretische Festkörperphysik* (Springer, 2008).

[43] S. Reich, C. Thomsen and J. Maultzsch, *Carbon Nanotubes: Basic Concepts and Physical Properties* (Wiley-VCH, 2004).

[44] R. Saito, G. Dresselhaus and M. S. Dresselhaus, *Physical properties of carbon nanotubes* (Imperial College, 2005).

[45] A. Jorio, M. Dresselhaus and G. Dresselhaus, *Carbon nanotubes: advanced topics in the synthesis, structure, properties and applications* (Springer, 2008).

[46] J. Maultzsch, S. Reich, C. Thomson, H. Requardt and J. Ordejn, Phys. Rev. Lett. **92**, 75501 (2004).

[47] S. Piscanec, M. Lazzeri, F. Mauri, A. C. Ferrari, and J. Robertson, Phys. Rev. Lett. **93**, 185503 (2004).

[48] E. H. Hwang and S. Das Sarma, Phys. Rev. B **77**, 115449 (2008).

[49] W.-K. Tse and S. Das Sarma, Phys. Rev. B **79**, 235406 (2009).

[50] M. Kira and S. Koch, Progress in Quantum Electronics **30**, 155 (2006).

[51] J. Fricke, Annals of Physics **252**, 479 (1996).

[52] V. M. Axt and T. Kuhn, Rep. Prog. Phys. **67**, 433 (2004).

[53] W. W. Chow and S. W. Koch, *Semiconductor-Laser Fundamentals* (Springer, 1999).

[54] K. Kang, D. Abdula, D. G. Cahill, and M. Shim, Phys. Rev. B **81**, 165405 (2010).

[55] E. Wigner, Phys. Rev. **40**, 749 (1932).

[56] O. Hess and T. Kuhn, Phys. Rev. A **54**, 3347 (1996).

[57] D. Sun, C. Divin, M. Mihnev, T. Winzer, E. Malic, A. Knorr, J. E. Sipe, C. Berger, W. A. de Heer, P. N. First, and T. B. Norris, New J. Phys. **14**, 105012 (2012).

[58] T. Meier, G. von Plessen, P. Thomas, and S. W. Koch, Phys. Rev. Lett. **73**, 902 (1994).

[59] J. D. Jackson, *Classical Electrodynamics* (Wiley, 1998).

[60] S. Butscher, F. Milde, M. Hirtschulz, E. Malic, and A. Knorr, Appl. Phys. Lett. **91**, 203103 (2007).

[61] J. M. Dawlaty, S. Shivaraman, M. Chandrashekhar, F. Rana, and M. G. Spencer, Appl. Phys. Lett. **92**, 042116 (2008).

[62] P. Plochocka, P. Kossacki, A. Golnik, T. Kazimierczuk, C. Berger, W. A. de Heer, and M. Potemski, Phys. Rev. B **80**, 245415 (2009).

[63] M. T. Mihnev, F. Kadi, C. J. Divin, T. Winzer, S. Lee, C.-H. Liu, Z. Zhong, C. Berger, W. A. de Heer, E. Malic, A. Knorr, and T. B. Norris, Nature Commun. **7** (2016).

[64] M. Hirtschulz, E. Milde, F.and Malic, S. Butscher, C. Thomsen, S. Reich, and A. Knorr, Phys. Rev. B **77**, 035403 (2008).

[65] C. Köhler, T. Watermann, and E. Malic, J. Phys.: Condens. Matter **25**, 105301 (2013).

[66] M. Feierabend, G. Berghäuser, A. Knorr, and E. Malic, Nature Commun. **8** (2017).

[67] E. Malic, M. Selig, M. Feierabend, S. Brem, D. Christiansen, F. Wendler, A. Knorr, and G. Berghäuser, Phys. Rev. Materials **2**, 014002 (2018).

[68] S. Brem, M. Selig, G. Berghaeuser, and E. Malic, Sci. Rep. **8** (2018).

[69] S. Winnerl, M. Orlita, P. Plochocka, P. Kossacki, M. Potemski, T. Winzer, E. Malic, A. Knorr, M. Sprinkle, C. Berger, W. A. de Heer, H. Schneider, and M. Helm, Phys. Rev. Lett. **107**, 237401 (2011).

[70] T. Li, L. Luo, M. Hupalo, J. Zhang, M. C. Tringides, J. Schmalian and J. Wang, Phys. Rev. Lett. **108**, 167401 (2012).

[71] I. Gierz, J. C. Petersen, M. Mitrano, C. Cacho, I. C. E. Turcu, E. Springate, A. Stöhr, A. Köhler, U. Starke, and A. Cavalleri, Nature Mater. **12**, 1119 (2013).

[72] V. Ryzhii, M. Ryzhii, and T. Otsuji, J. Appl. Phys. **101**, 083114 (2007).

[73] T. Winzer, E. Malic, and A. Knorr, Phys. Rev. B **87**, 165413 (2013).

[74] S. Brem, F. Wendler, and E. Malic, Phys. Rev. B **96**, 045427 (2017).

[75] S. Brem, F. Wendler, S. Winnerl, and E. Malic, Phys. Rev. Materials **2**, 034002 (2018).

[76] A. B. Kashuba, Phys. Rev. B **78**, 085415 (2008).

[77] L. Fritz, J. Schmalian, M. Müller, and S. Sachdev, Phys. Rev. B **78**, 085416 (2008).

[78] I. V. Gornyi, V. Y. Kachorovskii, and A. D. Mirlin, Phys. Rev. B **86**, 165413 (2012).

[79] R. Bistritzer and A. H. MacDonald, Phys. Rev. B **80**, 085109 (2009).

[80] O. G. Balev, F. T. Vasko, and V. Ryzhii, Phys. Rev. B **79**, 165432 (2009).

[81] S. Tani, F. Blanchard, and K. Tanaka, Phys. Rev. Lett. **109**, 166603 (2012).

[82] B. Dóra and R. Moessner, Phys. Rev. B **81**, 165431 (2010).

[83] B. Rosenstein, M. Lewkowicz, H. C. Kao, and Y. Korniyenko, Phys. Rev. B **81**, 041416 (2010).

[84] J. Schwinger, Phys. Rev. **82**, 664 (1951).

[85] G. Konstantatos, M. Badioli, L. Gaudreau, J. Osmond, M. Bernechea, F. P. G. de Arquer, F. Gatti, and F. H. L. Koppens, Nat. Nano. **7**, 363 (2012).

[86] C.-H. Liu, Y.-C. Chang, T. B. Norris, and Z. Zhong, Nat. Nano. **9**, 273 (2014).

[87] L. Huang, G. V. Hartland, L.-Q. Chu, Luxmi, R. M. Feenstra, C. Lian, K. Tahy, and H. Xing, Nano Letters **10**, 1308 (2010).

[88] R. Rengel, E. Pascual, and M. J. Martin, Applied Physics Letters **104**, 233107 (2014).

[89] Y. Ishida, H. Masuda, H. Sakai, S. Ishiwata, and S. Shin, Phys. Rev. B **93**, 100302 (2016).

[90] J. H. Grönqvist, M. Hirtschulz, A. Knorr, and M. Lindberg, Phys. Rev. B **81**, 035414 (2010).

[91] T. Kato and T. Kaneko, ACS Nano **10**, 9687 (2016).

[92] L. Yuan, T. Wang, T. Zhu, M. Zhou, and L. Huang, J. Phys. Chem. Lett. **8**, 3371 (2017).

[93] R. Rosati, F. Lengers, D. E. Reiter, and T. Kuhn, Phys. Rev. B **98**, 195411 (2018).

[94] M. Kulig, J. Zipfel, P. Nagler, S. Blanter, C. Schüller, T. Korn, N. Paradiso, M. M. Glazov, and A. Chernikov, Phys. Rev. Lett. **120**, 207401 (2018).

[95] R. Pathria and P. Beale, in *Statistical Mechanics (Third Edition)* (Academic Press, 2011).

[96] B. A. Ruzicka, S. Wang, L. K. Werake, B. Weintrub, K. P. Loh, and H. Zhao, Phys. Rev. B **82**, 195414 (2010).

[97] B. A. Ruzicka, S. Wang, J. Liu, K.-P. Loh, J. Z. Wu, and H. Zhao, Opt. Mater. Express **2**, 708 (2012).

[98] A. Einstein, Annalen der Physik **322**, 549 (1905).

[99] D. B. Farmer, V. Perebeinos, Y.-M. Lin, C. Dimitrakopoulos, and P. Avouris, Phys. Rev. B **84**, 205417 (2011).

[100] W. Zhu, V. Perebeinos, M. Freitag, and P. Avouris, Phys. Rev. B **80**, 235402 (2009).